

Published in final edited form as:

*Electromagn Waves (Camb)*. 2014 ; 147: 1–22.

## Photoacoustic tomography: principles and advances

Jun Xia<sup>1,†</sup>, Junjie Yao<sup>1,†</sup>, and Lihong V. Wang<sup>1,\*</sup>

<sup>1</sup>Optical Imaging Laboratory, Department of Biomedical Engineering, Washington University in St. Louis, One Brookings Drive, St. Louis, Missouri 63130, USA

### Abstract

Photoacoustic tomography (PAT) is an emerging imaging modality that shows great potential for preclinical research and clinical practice. As a hybrid technique, PAT is based on the acoustic detection of optical absorption from either endogenous chromophores, such as oxy-hemoglobin and deoxy-hemoglobin, or exogenous contrast agents, such as organic dyes and nanoparticles. Because ultrasound scatters much less than light in tissue, PAT generates high-resolution images in both the optical ballistic and diffusive regimes. Over the past decade, the photoacoustic technique has been evolving rapidly, leading to a variety of exciting discoveries and applications. This review covers the basic principles of PAT and its different implementations. Strengths of PAT are highlighted, along with the most recent imaging results.

### Keywords

Photoacoustic tomography; photoacoustic microscopy; photoacoustic computed tomography; vascular imaging; anatomical imaging; functional imaging; molecular imaging; brain imaging; tumor imaging; nanoparticle; super resolution

## 1. INTRODUCTION

With recent advances in photonics and optical molecular probes, optical imaging plays an increasingly important role in preclinical and clinical imaging. A fundamental constraint of optical imaging is light diffusion, which limits the spatial resolution in deep-tissue imaging. In the past decade, photoacoustic (PA) tomography (PAT) has emerged as a promising modality that overcomes this challenge [1, 2]. PAT capitalizes on the photoacoustic effect, which converts absorbed optical energy into acoustic energy. Because acoustic waves scatter much less than optical waves in tissue, PAT can generate high-resolution images in both the optically ballistic and diffusive regimes. With signals originating from optical absorption, PAT readily takes advantage of rich endogenous and exogenous optical contrasts. For instance, endogenous oxy- and deoxy-hemoglobin can serve as anatomical and functional contrasts for imaging vascular structures, hemoglobin oxygen saturation (sO<sub>2</sub>) [3], the speed of blood flow [4], and the metabolic rate of oxygen [5]. A broad choice of exogenous contrasts, including dyes [6, 7], nanoparticles [8–10], and reporter genes [11, 12], can be used for molecular imaging. In molecular PAT, molecular images are naturally co-registered

\*Corresponding author: lhwang@wustl.edu.

†These authors contributed equally.

with high-resolution anatomical/vascular images, enabling precise localization of the molecular process. Compared with other mainstream biomedical imaging modalities, the merits of PAT can be summarized as follows. (1) Compared with purely optical tomography, such as diffuse optical tomography (DOT) and fluorescence tomography (FMT), PAT can penetrate deeper and sustain high spatial resolution within the entire field of view. (2) Compared with ultrasonic imaging, PAT has rich intrinsic and extrinsic optical contrasts and is free of speckle artifacts. (3) Compared with X-ray computed tomography (X-ray CT) and positron emission tomography (PET), PAT uses nonionizing laser illumination. (4) Compared with magnetic resonance imaging (MRI), PAT is faster and less expensive. These unique advantages position PAT to make a broad impact in preclinical studies and clinical practice.

Over the past ten years, PAT has been evolving rapidly, and applications of PAT have been established in vascular biology [13–16], oncology [17–24], neurology [25–29], ophthalmology [30–34], dermatology [35–39], gastroenterology [40–44], and cardiology [37, 45–47]. The purpose of this review is to provide a general overview of the PAT technique. The second section covers the fundamental principles of PAT, including signal generation and image formation. The third section introduces the two major implementations of PAT, photoacoustic computed tomography (PACT) and photoacoustic microscopy (PAM). The last section highlights the strengths of PAT and describes the most recent advances.

## 2. PRINCIPLES OF PHOTOACOUSTIC TOMOGRAPHY

### 2.1. Signal generation in PAT

As mentioned previously, PAT signals originate from optical absorption. The process of photoacoustic signal generation can be described in three steps: (1) an object absorbs light, (2) the absorbed optical energy is converted into heat and generates a temperature rise, and (3) thermoelastic expansion takes place, resulting in the emission of acoustic waves. Typical endogenous tissue chromophores (optical absorbers) include hemoglobin, melanin, and water. As shown in Figure 1, the optical absorption coefficients are sensitive to wavelength, and thus the concentration of each chromophore can be extracted through spectroscopic inversion. For instance, functional photoacoustic imaging of sO<sub>2</sub> relies on the absorption difference between oxy-hemoglobin (HbO<sub>2</sub>) and deoxy-hemoglobin (HbR) [3].

To generate acoustic waves, the thermal expansion needs to be time variant. This requirement can be achieved by using either a pulsed laser [48] or a continuous-wave (CW) laser with intensity modulation at a constant [49] or variable frequency [50]. Pulsed excitations are the most widely used because they provide a higher signal to noise ratio than CW excitations, if both use the maximum allowable fluence or power set by the American National Standards Institute (ANSI) [49, 51, 52]. Following a short laser pulse excitation, the local fractional volume expansion  $dV/V$  can be expressed as

$$\frac{dV}{V} = -\kappa p(\vec{r}) + \beta T(\vec{r}), \quad (1)$$

where  $\kappa$  is the isothermal compressibility,  $\beta$  is the thermal coefficient of volume expansion, and  $p(\vec{r})$  and  $T(\vec{r})$  are changes in pressure and temperature, respectively.

For effective PAT signal generation, the laser pulse duration is normally within several nanoseconds, which is less than both the thermal and stress confinement times. The thermal confinement indicates that thermal diffusion during laser illumination can be neglected, i.e., [53]

$$\tau < \tau_{th} = \frac{d_c^2}{4D_T}, \quad (2)$$

Here,  $\tau_{th}$  is the thermal confinement threshold,  $d_c$  is the desired spatial resolution, and  $D_T$  is the thermal diffusivity ( $\sim 0.14 \text{ mm}^2/\text{s}$  for soft tissue [54]).

The stress confinement means the volume expansion of the absorber during the illumination period can be neglected. This condition can be written as

$$\tau < \tau_{st} = \frac{d_c}{v_s}, \quad (3)$$

where  $v_s$  is the speed of sound.

For a  $100 \mu\text{m}$  spatial resolution, the thermal confinement time is 18 ms and the stress confinement time is 67 ns. A typical pulsed laser has a pulse duration of only 10 ns. In this case, the fractional volume expansion in Eq. (1) is negligible and the initial photoacoustic pressure  $p_0(\vec{r})$  can be written as

$$p_0(\vec{r}) = \frac{\beta T(\vec{r})}{\kappa}. \quad (4)$$

For soft tissue,  $\kappa$  is approximately  $5 \times 10^{-10} \text{ Pa}^{-1}$  and  $\beta$  is around  $4 \times 10^{-4} \text{ K}^{-1}$ . Thus each mK temperature rise generates a 800 Pa pressure rise, which is detectable ultrasonically. The temperature rise can be further expressed as a function of optical absorption,

$$T = \frac{A_e}{\rho C_V}. \quad (5)$$

Here  $\rho$  is the mass density,  $C_V$  is the specific heat capacity at constant volume, and  $A_e$  is the absorbed energy density, which is a product of the absorption coefficient  $\mu_a$  and the local optical fluence  $F(\vec{r})$ .

Based on Eqs. (4) and (5), the initial photoacoustic pressure can be written as

$$p_0(\vec{r}) = \frac{\beta A_e}{\rho C_V \kappa} = \Gamma \mu_a F(\vec{r}). \quad (6)$$

Here  $\Gamma(\vec{r}) = \frac{\beta}{\rho C_V \kappa}$  is the Grueneisen parameter, which increases as the temperature rises. Thus PAT can also be used to monitor temperature [55, 56]. Eq. (6) indicates that, to extract

the object's absorption coefficient from pressure measurements, the local fluence  $F(\vec{r})$  needs to be quantified.

Once the initial pressure  $p_0(\vec{r})$  is generated, it splits into two waves with equal magnitude, traveling in opposite directions. The shape of the wavefront depends on the geometry of the object. For a spherical object, two spherical waves will be generated: one travels outward, and the other travels inward as compression followed by rarefaction. Thus the photoacoustic signal has a bipolar shape and the distance between the two peaks is proportional to the size of the object. In other words, a smaller object generates a photoacoustic signal with higher frequency components.

The generated photoacoustic pressure propagates through the sample and is detected by an ultrasonic transducer or transducer array. The goal of photoacoustic image formation is to recover the distribution of  $p_0(\vec{r})$  from the time-resolved ultrasonic signals.

## 2.2. Image formation in PAT

Based on the image formation methods, PAT has two major implementations [2]. The first, direct image formation, is based on mechanical scanning of a focused single-element ultrasonic transducer, and is commonly used in photoacoustic microscopy (PAM). The second, reconstruction image formation, is based on mechanical/electronic scanning of a multi-element transducer array, and is used in photoacoustic computed tomography (PACT). In PAM, the received photoacoustic signal originates primarily from the volume laterally confined by the acoustic focus and can be simply converted into a one-dimensional image along the acoustic axis. In PACT, each transducer element has a large acceptance angle within the field of view, and a PA image can only be reconstructed only by merging data from all transducer elements. In the following, we will discuss PACT image reconstruction in detail.

For an ideal point transducer placed at  $r_d$ , the detected photoacoustic signal can be written as [57]

$$p_d(\vec{r}_d, t) = \frac{\partial}{\partial t} \left[ \frac{t}{4\pi} \iint_{|\vec{r}_d - \vec{r}| = v_s t} p_0(\vec{r}) d\Omega \right]. \quad (7)$$

Here,  $d\Omega$  is the solid-angle element of  $r$  with respect to the point at  $r_d$ , and  $v_s$  is the speed of sound. Eq. (7) indicates that the detected pressure at time  $t$  comes from sources over a spherical shell centered at the detector position  $r_d$  with a radius  $v_s t$ . The initial pressure distribution  $p_0(\vec{r})$  can be obtained by inverting Eq. (7). For spherical, planar, and cylindrical detection geometries, exact inversion solutions have been provided by Xu *et al.* [57]. The so-called universal back-projection (UBP) algorithm can be expressed in the temporal domain as [58]:

$$p_0(\vec{r}) = \frac{1}{\Omega_0} \int_s d\Omega \left[ 2p_d(\vec{r}_d, t) - 2t \frac{\partial p_d(\vec{r}_d, t)}{\partial t} \right] \Bigg|_{t=|\vec{r}_d - \vec{r}|/C}. \quad (8)$$

Here,  $\Omega_0$  is the solid angle of the whole detection surface  $S$  with respect to a given source point at  $r$ . Eq. (8) indicates that  $p_0(r)$  can be obtained by back-projecting the filtered data,

$\left[ 2p_d(\vec{r}_d, t) - 2t \frac{\partial p(\vec{r}_d, t)}{\partial t} \right]$ , onto a collection of concentric spherical surfaces that are centered at each transducer location  $r_d$ , with  $d\Omega/\Omega_0$  as the weighting factor applied to each back-projection.

A variety of other reconstruction algorithms have also been developed [59–61]. Among them, the time-reversal (TR) method is the least restrictive [62], as it can be applied to arbitrarily closed surfaces and can incorporate acoustic heterogeneities, such as variations in speed of sound and acoustic attenuation [61, 63]. In the TR method, the measured acoustic waves are retransmitted in a temporally reversed order. This procedure is done by solving the wave propagation model backwards from  $t = T$  to  $t = 0$ , using the measured data as the boundary condition. Here  $T$  is the maximum time for the wave to traverse the detection domain. Solving such an equation requires numerical methods, such as finite-difference techniques [64]. Compared to UBP, TR is computationally more intensive, as it needs to compute the wavefield within the entire detection geometry. An open source MATLAB toolbox (k-Wave) for TR reconstruction has been made available by Treeby *et al.* [64].

Both UBP and TR algorithms assume idealized point-like ultrasonic transducers with a large acceptance angle and an infinite temporal-frequency bandwidth, which are practically unachievable. The impact of transducer characteristics on spatial resolution was first investigated by Xu *et al.* in 2003, who found that the bandwidth affects both axial and lateral resolutions, while the detector aperture mainly affects the lateral resolution [65]. In terms of reconstruction accuracy, directly applying UBP or TR algorithms to experimental data could be problematic because the transducer response acts as an additional filter to the original pressure. Recently, based on the transducer characteristics, advanced image reconstruction algorithms have been developed to provide more accurate images than UBP or TR [66, 67].

It should also be noted that, in practice, the detection surface can never be infinite and can hardly be closed. For instance, due to the chest wall, a spherical-view breast scanner can achieve only hemi-spherical coverage. As a consequence, only part of the photoacoustic wavefront is detected, yielding incomplete data. Such limited-view PACT normally suffers from missing or blurred boundaries [68]. In addition, the spatial sampling over the detection aperture could be insufficient, causing streaking artifacts or grating lobes [69]. A variety of algorithms have been proposed to improve the image quality of limited-view or under-sampled PACT. For instance, iterative image reconstruction algorithms have been developed to enhance the boundary sharpness [68]. For linear-array-based PACT systems, acoustic reflectors have been employed to redirect part of the photoacoustic wave back to the transducer, and thus improve the detection coverage [70]. When the target objects are sparse, compressed-sensing-based algorithms have been used in PACT to reduce the density of spatial sampling [69, 71].

### 3. PHOTOACOUSTIC TOMOGRAPHY SYSTEMS

#### 3.1. Photoacoustic computed tomography

As mentioned above, PACT has three canonical detection geometries: planar, cylindrical, and spherical. Each geometry has a variety of implementations. For a planar-view PACT system, the photoacoustic signal can be detected by either a 2D matrix piezoelectric transducer array [72] or a Fabry-Perot interferometer (FPI) (Figure 2a) [73, 74]. Ideally, each transducer element needs to be smaller than the acoustic wavelength in order to ensure a large receiving angle. In this regard, the FPI sensor is advantageous because of its high detection sensitivity and small element size, which is defined by the focal size of the probe beam. However, because the current FPI-based PACT system uses only one probe beam (Figure 2a), its imaging speed is much lower than that of a 2D-matrix-array-based PACT system [72]. Figure 2b shows an *in situ* image of the abdomen of a pregnant mouse, acquired by the FPI-based PACT system [75]. Two embryos (shaded red) can be clearly seen, along with the vasculature of the uterus and the skin.

Cylindrical-view PACT is commonly implemented by a ring-transducer array. To improve the cross-sectional imaging capability, each element in the array is usually cylindrically focused, and thus rejects out-of-plane signals. Strictly speaking, such a system is a circular-view PACT. However, a three-dimensional (3D) image can still be acquired by scanning the sample or array along the elevational direction. The 3D data can be reconstructed using a modified back projection algorithm, which accounts for the transducer's spatial response [76]. Compared to planar- and spherical-view PACT, which can perform only 3D imaging, circular-view PACT has both 2D and 3D imaging capabilities, and can be used for high-speed cross-sectional (2D) dynamic imaging [77]. Figure 3 shows a schematic of a ring-array-based small-animal imaging system and representative images [78]. Blood-rich organs, such as the liver, spleen, spine, kidneys, and gastrointestinal (GI) tract, are clearly visible. Detailed vascular structures within these organs are also visible, indicating that the system can be used for angiographic imaging.

A spherical-view PACT system can provide nearly isotropic spatial resolution within the central imaging region. There are multiple variations of spherical-view PACT, including an arc-shaped transducer array that scans around the object [80, 81] and a hemispherical transducer array with elements distributed in a spiral pattern [82, 83]. Both systems require mechanical scanning, and an image can be reconstructed only after a complete 3D scan, making real-time imaging challenging. Advanced image reconstruction algorithms, such as highly constrained back projection [82], have been proposed to allow dynamic imaging from highly under-sampled data. Figure 4a is a photograph of an arc-array-based spherical-view PACT system [80]. For a complete volumetric scan, the animal was rotated 360 degrees in 150 steps. The volumetric image (Figure 4b) clearly shows the left and right kidneys, the spleen, and a partial lobe of the liver. The inferior vena cava and its bifurcation into the femoral veins can be seen.

For all three detection geometries, the axial resolution is spatially invariant and is primarily determined by the bandwidth of the ultrasonic transducer [65]. For a wideband transducer, the axial resolution,  $a$ , approximates  $0.6\lambda_c$ , where  $\lambda_c$  is the acoustic wavelength at the high

cutoff frequency. The lateral resolution for spherical- and cylindrical-view PACTs can be characterized by  $\sqrt{a^2 + [(r/r_0)d]^2}$ , where  $r$  is the distance between the imaging point and the scanning center,  $r_0$  is the radius of the scan circle, and  $d$  is the width of each transducer element [84]. The lateral resolution for a planar-view PACT can be characterized by  $\sqrt{a^2 + d^2}$ .

### 3.2. Photoacoustic microscopy

Photoacoustic microscopy (PAM) is another major implementation of PAT, which images targets in the (quasi)ballistic and quasidiffusive regimes at high spatial resolution at depths [85]. Here, we define microscopy as an imaging modality with a spatial resolution finer than 50  $\mu\text{m}$ , since unaided eyes can discern only features larger than 50  $\mu\text{m}$ . As mentioned previously, the most significant difference between PAM and PACT is that PAM uses a focused single-element ultrasonic transducer for direct image formation, while PACT typically uses a multi-element transducer array or its equivalent for digital image reconstruction.

The lateral resolution of PAM is determined by the product of the point spread functions of the light illumination and acoustic detection [85]. The axial resolution of PAM is determined by the detection bandwidth of the ultrasonic transducer, which is chosen to match the acoustic path length due to frequency-dependent acoustic attenuation in tissue [85]. Based on the dominant determining factor for lateral resolution, PAM can be further classified into optical-resolution PAM (OR-PAM) and acoustic-resolution PAM (AR-PAM). In OR-PAM, the laser beam is tightly focused to a diffraction-limited spot, which is typically more than 10 times smaller in diameter than the acoustic focusing. Therefore, the lateral resolution of OR-PAM is primarily determined by the optical focal spot size (Figure 5a) [86, 87]. Since OR-PAM relies highly on the tight optical focusing, it can penetrate about one optical transport mean free path (TMFT) in tissue ( $\sim 1$  mm in muscle and  $\sim 0.6$  mm in the brain), limited by the strong optical scattering. In contrast, in AR-PAM, the excitation laser beam is only loosely focused to fulfill the entire acoustic detection volume (Figure 5b). In this case, the lateral resolution does not closely depend on the tissue's optical scattering characteristics, because it is the ultrasonic focusing that determines the lateral resolution at depths within a few TMFTs [3, 88]. As a variant of PAM miniaturized for internal organ imaging, photoacoustic endoscopy (PAE) is typically based on rotational scanning [89–93]. PAE can be configured in either optical-resolution [90] or acoustic-resolution modes [93].

By adjusting the optical illumination and/or acoustic detection configurations, PAM can scale in spatial resolution and penetration depth over a wide range [85]. Specifically, the lateral resolution of OR-PAM can be scaled down by either increasing the numerical aperture (NA) of the objective lens or using a shorter excitation wavelength, with the maximum imaging depth scaled accordingly. In comparison, the lateral resolution of AR-PAM can be scaled by varying the acoustic central frequency and the NA of the acoustic lens. Detailed reviews about PAM technologies can be found in two recent publications [2, 85].

## 4. STRENGTHS OF PAT

### 4.1. Multi-scale PAT

As a hybrid technique, PAT has the unique capability of scaling its spatial resolution and imaging depth across both optical and ultrasonic dimensions [2]. For OR-PAM, whose lateral resolution is mainly determined by the numerical aperture (NA) of the optical microscopic objective, a higher NA improves the lateral resolution, but decreases the imaging depth. For instance, a 1.23-NA OR-PAM system has a 0.22  $\mu\text{m}$  lateral resolution and 100  $\mu\text{m}$  imaging depth, while a 0.1-NA OR-PAM system has a 2.6  $\mu\text{m}$  lateral resolution and a 1.2 mm imaging depth [2]. In the optically diffusive region, the spatial resolution is acoustically defined. While a higher central frequency transducer provides a higher spatial resolution, the frequency-dependent acoustic attenuation ( $\sim 1$  dB/MHz/cm in muscle) limits the imaging depth. Thus an AR-PAM system normally employs a transducer with a central frequency greater than 20 MHz to provide a sub 100  $\mu\text{m}$  lateral resolution with an imaging depth of several millimeters. Low frequency ( $< 10$  MHz) transducers are commonly used in PACT systems to provide an imaging depth greater than 1 cm. Above 10 cm, the imaging depth is also limited by light attenuation, which is a combined effect of optical absorption and scattering. With recent advances in optical wave-front engineering [95, 96], we expect the attenuation through optical scattering to be minimized, and PAT to eventually image tens of centimeters deep in tissue.

The multi-scale imaging capability of PAT was demonstrated by imaging the expression of *LacZ*, a widely used reporter gene in molecular imaging [97]. It encodes  $\beta$ -galactosidase, an *E. coli* enzyme responsible for metabolizing lactose into glucose and galactose. This enzyme also causes bacteria expressing the gene to appear blue when grown on a medium that contains the substrate analog X-gal [98]. The blue product has strong optical absorption at wavelengths from 605 nm to 665 nm, and thus provides a good contrast for deep PA imaging. The multi-scale PAT experiment was performed on a mouse with a subcutaneously inoculated tumor. To demonstrate the imaging depth, multiple pieces of chicken breast tissues were overlaid on the tumor, and photoacoustic images were acquired by a linear ultrasound transducer array with 4 – 8 MHz bandwidth [99]. Figure 6a is a composite photoacoustic and ultrasound B-mode image. It can be seen that the expression of *LacZ* remained visible at a depth of 5 cm in biological tissue. The tumor-to-background contrast was found to be 3 [99]. The chicken breast tissues were then removed, and the mouse was imaged using the AR-PAM system with a 45  $\mu\text{m}$  lateral resolution and a 15  $\mu\text{m}$  axial resolution. Two laser wavelengths, 635 nm and 584 nm, were used to maximize the difference between the optical absorption of hemoglobin and the blue product. The combined image in Figure 6b clearly shows the spatial relation between the tumor and the surrounding microvasculature. An OR-PAM system was also used. Figure 6c shows fixed *lacZ* cells grown on a cover glass after staining with X-gal. With a spatial resolution of 0.4  $\mu\text{m}$ , the *lacZ* cell structure can be resolved. Strong absorbers can be seen around the low absorbing center (cell nuclei), indicating that the blue product exists mostly in the cytoplasm.

This study demonstrates that PAT can image reporter genes from the microscopic to the macroscopic scales. Currently multi-scale PAT imaging is performed using different PAT systems. With the introduction of optical-resolution photoacoustic computed microscopy [100], which achieves optical-resolution imaging in a PACT system, multi-scale PAT images can potentially be acquired using a single setup.

#### 4.2. Super-resolution PAT

Super-resolution imaging has opened new possibilities for fundamental biological studies. With resolutions finer than the optical diffraction limit ( $\sim 250$  nm in lateral direction at high optical NA), super-resolution imaging has enabled observations of cellular and subcellular structures and processes that are unresolvable by conventional microscopes [101]. However, most of the existing super-resolution imaging techniques can perform only fluorescence imaging by using multiple lasers and/or chemical manipulation of fluorophores, resulting in complex system configurations and strict requirements for the fluorescent targets. PAT, on the other hand, can potentially image both fluorescent and nonfluorescent molecules at appropriate wavelengths. Recently, progress has been made to break the diffraction limits in PAT for super-resolution imaging.

In OR-PAM, Yao *et al.* overcame the optical-diffraction limit by using the excitation-intensity dependence of the photobleaching effect (Figure 7a–b) [102]. Within the optical focal spot, molecules in the center part of the illuminated region are bleached more than those in the periphery, leaving an imprint in the sample. The pixel-by-pixel differences between the image acquired before and after the bleaching highlight the central region of the excitation spot. Sub-diffraction PA imaging of gold nanoparticles has been demonstrated with a resolution of  $\sim 80$  nm, three times smaller than the optical diffraction limit. Another sub-optical-diffraction PA imaging method was reported by Nedosekin *et al.*, with a resolution of  $\sim 100$  nm for nanoparticles, where nonlinear signal amplification by nanobubbles circumvented the optical diffraction limit [103]. In this method, the center region of the excitation spot generated nanobubbles with greater sizes than the periphery. Collapse of the nanobubbles enhanced the PA signals non-uniformly across the excitation field, highlighting the center region.

In addition to the sub-optical-diffraction imaging in the optical (quasi)ballistic regime in ORPAM, sub-acoustic-diffraction imaging in the optical diffusive regime has also been achieved in AR-PAM. Conkey *et al.* and Lai *et al.* reported sub-acoustic-diffraction imaging methods using the photoacoustic signal as feedback for wavefront shaping optimization [104, 105]. Conkey *et al.*'s method takes advantage of the Gaussian-shape detection sensitivity of a focused ultrasonic transducer (Figure 7c–e). Photoacoustic imaging behind a scattering medium was demonstrated with a resolution of  $\sim 13$   $\mu\text{m}$ , five to six times smaller than the acoustic diffraction limit [104]. Based on the Grueneisen memory effect, Lai *et al.*'s method utilizes nonlinear PA signals as feedback to guide iterative wavefront optimization [105]. Experimental results demonstrated an optical diffraction-limited focus on the scale of 5–7  $\mu\text{m}$  in scattering media, ten times smaller than the acoustic diffraction limit, with an enhancement factor of  $\sim 6,000$  in peak fluence [105].

### 4.3. Multi-parameter PAT

PA signals can be used to derive a number of anatomical, functional, and metabolic parameters of the tissue microenvironment. Since a single parameter may not be able to fully reflect the true physiological and pathological conditions, multi-parameter PA imaging can potentially provide more comprehensive information for diagnosis, staging, and treatment of diseases. Here, we will review a few representative parameters that can be measured by PAT, together with the corresponding technologies.

For hemoglobin, the total concentration ( $C_{\text{Hb}}$ ) and oxygen saturation ( $s\text{O}_2$ ) are the most commonly used indexes of blood perfusion and oxygenation, respectively. In particular, increased  $C_{\text{Hb}}$  due to angiogenesis and decreased  $s\text{O}_2$  due to hypoxia are both hallmarks of late stage cancers, while hyperoxia is associated with early-stage cancers (Figure 8) [5, 106]. From fluence-compensated PA measurements at the isosbestic wavelengths of hemoglobin (498 nm, 568 nm, and 794 nm), the PA signal amplitude reflects the  $C_{\text{Hb}}$  distribution, regardless of the oxygenation level [5]. From fluence-compensated PA measurements at two or more wavelengths, the relative concentrations of the two forms of hemoglobin ( $\text{HbO}_2$  and  $\text{HbR}$ ) can be quantified through spectral analysis, and thus  $s\text{O}_2$  can be computed [5, 101, 107–112]. In practice, however, accurate laser fluence compensation for absolute  $C_{\text{Hb}}$  and  $s\text{O}_2$  quantification can be very challenging, especially for AR-PAM and PACT. A potential solution is to incorporate PAT with diffuse reflectance spectroscopy [113] or diffuse optical tomography (DOT) [114], which can quantify the tissue's optical properties or the fluence distribution. Alternatively, the frequency spectra of PA signals at multiple optical wavelengths can be used to fit for absolute concentrations of  $\text{HbO}_2$  and  $\text{HbR}$ , and thus  $C_{\text{Hb}}$  and  $s\text{O}_2$ , where fluence compensation is not required [115, 116]. Recently, another calibration-free method for absolute  $s\text{O}_2$  quantification in PACT has been developed by Xia *et al.*, based on the dynamics of the PA signals at different oxygenation states [117].

Using the excellent absorption contrast between intra- and extra-vascular spaces provided by hemoglobin, PAT can be employed to measure blood flow [109, 111, 118–120]. So far, a number of methods have been developed for PA measurement of blood flow speed. Similar to Doppler ultrasound, photoacoustic Doppler flowmetry measures the axial flow speed on the basis of Doppler frequency shift [4, 121, 122]. Correlation-based photoacoustic flowmetry measures the transverse or axial flow speeds by performing either temporal autocorrelation [18, 123–126] or cross-correlation [127] over consecutive photoacoustic waveforms, respectively. Photoacoustic thermal flowmetry can measure flow speed based on thermal convection [128]. Similarly, PA imaging of wash-in and wash-out dynamics of nanoparticles or organic dyes can also provide flow information [129–131]. Another method, developed by Zhang *et al.*, measures the flow speed in a homogenous medium, based on structured illumination and the Doppler frequency shift induced by the flowing medium [132]. However, all of the above methods have difficulty in deep flow measurement, because they all rely on resolvable particles in the media or clearly defined illumination patterns. This issue has recently been solved by thermally tagging the flowing medium using a HIFU (high-intensity focused ultrasound) transducer and detecting the tagged medium using AR-PAM and PACT [56, 133]. Blood flow under a 5-mm-thick layer of chicken tissue was measured with a sensitivity of 0.25 mm/s [56].

The metabolism of oxygen and glucose directly reflects tissue functioning. Almost all diseases, especially cancers, manifest abnormal oxygen and glucose metabolisms [106, 134]. Currently, OR-PAM can noninvasively quantify absolute oxygen metabolism using endogenous contrast [5, 135]. Alternatively, PAM can be integrated with Doppler OCT or Doppler ultrasound for oxygen metabolism quantification, where PAM is used for blood oxygenation measurement, while Doppler OCT or Doppler ultrasound quantifies blood flow [136, 137]. Further, by integrating fine spatial and temporal scales, single-cell PA flowoxigraphy, a new implementation of OR-PAM, is capable of imaging oxygen release from single red blood cells (RBCs) *in vivo* [138].

Although glucose has been explored as an endogenous contrast agent for PAT measurement of blood sugar levels, the detection sensitivity is still insufficient for clinical diagnosis [139]. Recently, two glucose analogs, 2-NBDG and IRDye-800-DG, have been used to noninvasively quantify glucose metabolism in mice. Similar to the FDG used in PET, 2-NBDG and IRDye-800-DG are transported into cells but cannot be further metabolized. Therefore, the distribution of the trapped glucose analogs reflects the glucose uptake and thus the local glucose metabolism. PACT with 2-NBDG and IRDye-800-2DG was used to study mouse brain metabolism and tumor hypermetabolism, respectively [132].

In addition to the above major functional and metabolic parameters, PAT can also measure a number of other tissue properties. Although some of these parameters can be obtained by fluorescence imaging as well, PAT can achieve deeper penetration at high spatial resolution than its fluorescence counterpart. PAT can also measure the temperature distribution in thermotherapy by using the temperature dependence of the Grueneisen parameter in deep tissue [55, 132] or in single cells [140]. PAT is capable of measuring overtone vibrational absorption in the near-infrared spectral region, which can reveal the tissue composition, such as lipids [141]. Similarly, PAT can be combined with stimulated Raman excitation for enhanced chemical specificity [142]. In addition, PAT has been used for imaging Förster resonance energy transfer (FRET), the efficiency of which reflects intra- and inter-molecular distances in the 1 to 10 nm range [143, 144]. PAT can measure the nonradiative absorption relaxation time of molecules by fitting the saturation curve of the signal amplitude as a function of incident laser intensity [145, 146]. Two other material parameters, dichroism [147] and magnetomotion [8, 148], can be used by PAT to enhance imaging specificity. In addition to absorber properties, PAT can also measure the microenvironment's properties, including pH and partial oxygen pressure ( $pO_2$ ), by using appropriate contrast agents [149–152].

#### 4.4. Molecular PAT

Endogenous PA contrasts, such as hemoglobin in red blood cells, melanin in melanoma cells, DNA/RNA in cell nuclei, water in brain edema, and lipids in myelin, are abundant and nontoxic. However, they may lack the requisite specificity for diagnosing disease or tracking biological processes. By using exogenous contrasts, molecular PAT enables visualizing specific cellular functions and molecular processes. In recent years, great efforts have been devoted to enhance the molecular imaging capability of PAT, and considerable progress has been made in optimizing both the PAT imaging systems for better detection sensitivity, and

the contrast agents for better contrast enhancement [153–155]. PAT has proven capable of high sensitivity molecular imaging by using various exogenous contrast agents, including microbubbles, organic dyes, nanoparticles, fluorescent proteins, and reporter gene products [156]. For example, one of the very first demonstrations of molecular PAT was to use IRDye800-c(KRGDf) to target overexpressed integrin  $\alpha_v\beta_3$  in brain glioblastoma (Figure 9a) [23]. Because of their dramatically different optical absorbing properties, the reported PA detection sensitivity for exogenous contrast agents varies from millimolar to picomolar [85, 157].

Compared with organic dyes, nanoparticles can be easily engineered for PA molecular imaging by tuning their size, shape, and composition for the optimum peak absorption wavelength [155]. Numerous nanoparticles have been used for PA molecular imaging, especially in cancer detection [159] and sentinel lymph node mapping [157]. For example, Kircher *et al.* have recently developed a brain tumor molecular imaging method using triple-modality MRI-photoacoustic- Raman nanoparticles (Figure 9b) [158]. A high detection sensitivity of 50 pM was achieved with an incident laser energy of only 8 mJ/cm<sup>2</sup>.

PAT of reporter gene products has also attracted more and more attention. A significant advantage of reporter gene products is that they are expressed in living cells and do not need complex exogenous delivery. So far, various fluorescent genetically encoded proteins have been explored for PA molecular imaging, such as mCherry, EGFP, iRFP, and RFP [12, 160–162]. Nonfluorescent gene products can also be imaged by PAT. For example, given the strong optical absorption of melanin, tyrosinase genes were transferred to non-melanogenic cells to encode eumelanin as the contrast agent for PA imaging [52, 54, 163, 164].

## 5. CONCLUSION

Over the last decade, the PAT technique has been evolving rapidly toward higher spatial resolution, higher frame rates, and higher detection sensitivity. The applications of PAT have also expanded greatly in fundamental life sciences, and many clinical applications have been proposed. The accelerating progress in PAT has also triggered growing contributions from biology, chemistry, and nanotechnology. With the commercialization of several PAT systems, we expect that PAT will become a mainstream imaging modality in the lab and clinic.

While exciting images have been acquired, PAT still faces limitations. For instance, the light attenuation limits the ultimate imaging depth. Currently, the maximum demonstrated PAT imaging depth is 8.4 cm in chicken breast tissue [39]. To address this limitation, novel light illumination schemes have been explored. For instance, by illuminating the object from both sides [41, 78], the imaging region can be doubled and potentially reach 16.4 cm. Internal light delivery has also been proposed to image organs far beneath the skin [165]. In terms of imaging speed, both PACT and PAM are currently limited by the pulse repetition rate of lasers. With advances in laser technology, we expect the PAT imaging speed to be improved accordingly. Quantitative PA imaging also faces challenges because of the difficulty in measuring local fluence distribution. Advanced spectral separation algorithms have been

proposed to address this issue [116, 117, 166]. Novel contrast agents have also been explored to improve the specificity of deep-tissue molecular photoacoustic imaging [8, 10].

Nevertheless, exciting PAT images have already been reported, and addressing the aforementioned challenges will only further improve the capability of PAT. With its unique combination of optical absorption contrast and ultrasonic imaging depth and resolution scalability [9], PAT is expected to find more high-impact applications in both biomedical research and clinical practice.

## CITATIONS

1. Wang LV. Multiscale photoacoustic microscopy and computed tomography. *Nat Photon.* 2009; 3:503–509.
2. Wang LV, Hu S. Photoacoustic Tomography: In Vivo Imaging from Organelles to Organs. *Science.* 2012 Mar 23.335:1458–1462. 2012. [PubMed: 22442475]
3. Zhang HF, Maslov K, Stoica G, Wang LV. Functional photoacoustic microscopy for high-resolution and noninvasive in vivo imaging. *Nat Biotech.* 2006; 24:848–851.
4. Fang H, Maslov K, Wang LV. Photoacoustic Doppler effect from flowing small light-absorbing particles. *Physical Review Letters.* 2007 Nov 2.99:184501. [PubMed: 17995411]
5. Yao J, Maslov KI, Zhang Y, Xia Y, Wang LV. Label-free oxygen-metabolic photoacoustic microscopy in vivo. *Journal of Biomedical Optics.* 2011 Jul.16:076003. [PubMed: 21806264]
6. Yao J, Xia J, Maslov KI, Nasirivanaki M, Tsytsarev V, Demchenko AV, Wang LV. Noninvasive photoacoustic computed tomography of mouse brain metabolism in vivo. *NeuroImage.* 2013; 64:257–266. [PubMed: 22940116]
7. Chatni MR, Xia J, Sohn R, Maslov K, Guo Z, Zhang Y, Wang K, Xia Y, Anastasio M, Arbeit J, Wang LV. Tumor glucose metabolism imaged in vivo in small animals with whole-body photoacoustic computed tomography. *Journal of Biomedical Optics.* 2012; 17:076012. [PubMed: 22894495]
8. Jin Y, Jia C, Huang S-W, O'Donnell M, Gao X. Multifunctional nanoparticles as coupled contrast agents. *Nat Commun.* 2010; 1:41. [PubMed: 20975706]
9. Lovell JF, Jin CS, Huynh E, Jin H, Kim C, Rubinstein JL, Chan WCW, Cao W, Wang LV, Zheng G. Porphysome nanovesicles generated by porphyrin bilayers for use as multimodal biophotonic contrast agents. *Nat Mater.* 2011; 10:324–332. [PubMed: 21423187]
10. Wilson K, Homan K, Emelianov S. Biomedical photoacoustics beyond thermal expansion using triggered nanodroplet vaporization for contrast-enhanced imaging. *Nature Communications.* 2012 Jan.3:10.
11. Razansky D, Distel M, Vinegoni C, Ma R, Perrimon N, Koster RW, Ntziachristos V. Multispectral opto-acoustic tomography of deep-seated fluorescent proteins in vivo. *Nat Photon.* 2009; 3:412–417.
12. Filonov GS, Krumholz A, Xia J, Yao J, Wang LV, Verkhusha VV. Deep-Tissue Photoacoustic Tomography of a Genetically Encoded Near-Infrared Fluorescent Probe. *Angewandte Chemie International Edition.* 2012; 51:1448–1451.
13. Oladipupo S, Hu S, Kovalski J, Yao JJ, Santeford A, Sohn RE, Shohet R, Maslov K, Wang LHV, Arbeit JM. VEGF is essential for hypoxia-inducible factor-mediated neovascularization but dispensable for endothelial sprouting. *Proceedings of the National Academy of Sciences of the United States of America.* 2011 Aug 9.108:13264–13269. [PubMed: 21784979]
14. Oladipupo SS, Hu S, Santeford AC, Yao JJ, Kovalski JR, Shohet RV, Maslov K, Wang LV, Arbeit JM. Conditional HIF-1 induction produces multistage neovascularization with stage-specific sensitivity to VEGFR inhibitors and myeloid cell independence. *Blood.* 2011 Apr 14.117:4142–4153. [PubMed: 21307392]
15. Bitton R, Zemp R, Yen J, Wang LV, Shung KK. A 3-D high-frequency array based 16 channel photoacoustic microscopy system for in vivo micro-vascular imaging. *IEEE Trans Med Imaging.* 2009 Aug.28:1190–1197. [PubMed: 19131292]

16. Xia J, Wang L. Small-animal whole-body photoacoustic tomography: a review. *Biomedical Engineering, IEEE Transactions on*. 2013:1–1. vol. PP.
17. Staley J, Grogan P, Samadi AK, Cui H, Cohen MS, Yang X. Growth of melanoma brain tumors monitored by photoacoustic microscopy. *Journal of Biomedical Optics*. 2010 Jul-Aug;15:040510. [PubMed: 20799777]
18. Chen SL, Ling T, Huang SW, Won Baac H, Guo LJ. Photoacoustic correlation spectroscopy and its application to low-speed flow measurement. *Optics Letters*. 2010 Apr 15.35:1200–1202. [PubMed: 20410966]
19. Cui HZ, Yang XM. In vivo imaging and treatment of solid tumor using integrated photoacoustic imaging and high intensity focused ultrasound system. *Medical Physics*. 2010 Sep.37:4777–4781. [PubMed: 20964197]
20. de la Zerda A, Liu ZA, Bodapati S, Teed R, Vaithilingam S, Khuri-Yakub BT, Chen XY, Dai HJ, Gambhir SS. Ultrahigh Sensitivity Carbon Nanotube Agents for Photoacoustic Molecular Imaging in Living Mice. *Nano Letters*. 2010 Jun.10:2168–2172. [PubMed: 20499887]
21. Li L, Zhang HF, Zemp RJ, Maslov K, Wang L. Simultaneous imaging of a lacZ-marked tumor and microvasculature morphology in vivo by dual-wavelength photoacoustic microscopy. *J Innov Opt Health Sci*. 2008 Oct 1.1:207–215. [PubMed: 19946613]
22. Li ML, Wang JC, Schwartz JA, Gill-Sharp KL, Stoica G, Wang LHV. In-vivo photoacoustic microscopy of nanoshell extravasation from solid tumor vasculature. *Journal of Biomedical Optics*. 2009 Jan-Feb;14:010507. [PubMed: 19256687]
23. Li M, Oh J-T, Xie X, Ku G, Wang W, Li C, Lungu G, Stoica G, Wang LV. Simultaneous Molecular and Hypoxia Imaging of Brain Tumors In Vivo Using Spectroscopic Photoacoustic Tomography. *Proceedings of the IEEE*. 2008; 96:481–489.
24. Olafsson R, Bauer DR, Montilla LG, Witte RS. Real-time, contrast enhanced photoacoustic imaging of cancer in a mouse window chamber. *Optics Express*. 2010 Aug 30.18:18625–18632. [PubMed: 20940754]
25. Hu S, Maslov K, Tsytsarev V, Wang LV. Functional transcranial brain imaging by optical-resolution photoacoustic microscopy. *Journal of Biomedical Optics*. 2009 Jul-Aug;14:040503. [PubMed: 19725708]
26. Wang XD, Ku G, Wegiel MA, Bornhop DJ, Stoica G, Wang LHV. Noninvasive photoacoustic angiography of animal brains in vivo with near-infrared light and an optical contrast agent. *Optics Letters*. 2004 Apr 1.29:730–732. [PubMed: 15072373]
27. Liao LD, Li ML, Lai HY, Shih YYI, Lo YC, Tsang SN, Chao PCP, Lin CT, Jaw FS, Chen YY. Imaging brain hemodynamic changes during rat forepaw electrical stimulation using functional photoacoustic microscopy. *Neuroimage*. 2010 Aug 15.52:562–570. [PubMed: 20362680]
28. Tsytsarev V, Hu S, Yao J, Maslov K, Barbour DL, Wang LV. Photoacoustic microscopy of microvascular responses to cortical electrical stimulation. *Journal of Biomedical Optics*. 2011 Jul. 16:076002. [PubMed: 21806263]
29. Nasirivanaki M, Xia J, Wan H, Bauer AQ, Culver JP, Wang LV. High-resolution photoacoustic tomography of resting-state functional connectivity in the mouse brain. *Proc Natl Acad Sci U S A*. 2014 Jan 7.111:21–26. [PubMed: 24367107]
30. Subach FV, Zhang LJ, Gadella TWJ, Gurskaya NG, Lukyanov KA, Verkhusha VV. Red Fluorescent Protein with Reversibly Photoswitchable Absorbance for Photochromic FRET. *Chemistry & Biology*. 2010 Jul 30.17:745–755. [PubMed: 20659687]
31. Jiao SL, Jiang MS, Hu JM, Fawzi A, Zhou QF, Shung KK, Puliafito CA, Zhang HF. Photoacoustic ophthalmoscopy for in vivo retinal imaging. *Optics Express*. 2010 Feb 15.18:3967–3972. [PubMed: 20389409]
32. Xie ZX, Jiao SL, Zhang HF, Puliafito CA. Laser-scanning optical-resolution photoacoustic microscopy. *Optics Letters*. 2009 Jun 15.34:1771–1773. [PubMed: 19529698]
33. Silverman RH, Kong F, Chen YC, Lloyd HO, Kim HH, Cannata JM, Shung KK, Coleman DJ. High-resolution photoacoustic imaging of ocular tissues. *Ultrasound Med Biol*. 2010 May.36:733–742. [PubMed: 20420969]
34. Song W, Wei Q, Liu T, Kuai D, Burke JM, Jiao S, Zhang HF. Integrating photoacoustic ophthalmoscopy with scanning laser ophthalmoscopy, optical coherence tomography, and

- fluorescein angiography for a multimodal retinal imaging platform. *Journal of Biomedical Optics*. 2012; 17:061206–061207. [PubMed: 22734736]
35. Zhang HF, Maslov K, Li ML, Stoica G, Wang LHV. In vivo volumetric imaging of subcutaneous microvasculature by photoacoustic microscopy. *Optics Express*. 2006 Oct 2.14:9317–9323. [PubMed: 19529315]
  36. Favazza CP, Cornelius LA, Wang LHV. In vivo functional photoacoustic microscopy of cutaneous microvasculature in human skin. *Journal of Biomedical Optics*. 2011 Feb.16:026004. [PubMed: 21361688]
  37. Favazza C, Jassim O, Wang LV, Cornelius L. In vivo photoacoustic microscopy of human skin. *Journal of Investigative Dermatology*. 2010 Apr.130:S145.
  38. Song LA, Maslov K, Shung KK, Wang LHV. Ultrasound-array-based real-time photoacoustic microscopy of human pulsatile dynamics in vivo. *Journal of Biomedical Optics*. 2010 Mar-Apr; 15:021303. [PubMed: 20459225]
  39. Favazza, C.; Maslov, K.; Cornelius, L.; Wang, LV. *Photons Plus Ultrasound: Imaging and Sensing 2010*. San Francisco, California, USA: 2010. In vivo functional human imaging using photoacoustic microscopy: response to ischemic and thermal stimuli; p. 75640Z-75640Z-6.
  40. Rowland KJ, Yao JJ, Wang LD, Erwin CR, Maslov KI, Wang LHV, Warner BW. Immediate alterations in intestinal oxygen saturation and blood flow after massive small bowel resection as measured by photoacoustic microscopy. *Journal of Pediatric Surgery*. 2012 Jun.47:1143–1149. [PubMed: 22703784]
  41. Yao J, Maslov KI, Puckett ER, Rowland KJ, Warner BW, Wang LV. Double-illumination photoacoustic microscopy. *Optics Letters*. 2012; 37:659–661. [PubMed: 22344139]
  42. Yang, J-M.; Chen, R.; Favazza, C.; Yao, J.; Zhou, Q.; Shung, KK.; Wang, LV. *Photons Plus Ultrasound: Imaging and Sensing 2012*. San Francisco, California, USA: 2012. A 2.5-mm outer diameter photoacoustic endoscopic mini-probe based on a highly sensitive PMN-PT ultrasonic transducer; p. 82233M-82233M-6.
  43. Yang, J-M.; Favazza, C.; Chen, R.; Yao, J.; Cai, X.; Maslov, K.; Zhou, Q.; Shung, KK.; Wang, LV. *Photons Plus Ultrasound: Imaging and Sensing 2012*. San Francisco, California, USA: 2012. Toward dual-wavelength functional photoacoustic endoscopy: laser and peripheral optical systems development; p. 822316-822316-7.
  44. Yao, J.; Rowland, KJ.; Wang, L.; Maslov, KI.; Warner, BW.; Wang, LV. *Photons Plus Ultrasound: Imaging and Sensing 2012*. San Francisco, California, USA: 2012. Double-illumination photoacoustic microscopy of intestinal hemodynamics following massive small bowel resection; p. 82233V-82233V-7.
  45. Taruttis A, Herzog E, Razansky D, Ntziachristos V. Real-time imaging of cardiovascular dynamics and circulating gold nanorods with multispectral photoacoustic tomography. *Optics Express*. 2010 Sep 13.18:19592–19602. [PubMed: 20940855]
  46. Zhang C, Maslov K, Wang LHV. Subwavelength-resolution label-free photoacoustic microscopy of optical absorption in vivo. *Optics Letters*. 2010 Oct 1.35:3195–3197. [PubMed: 20890331]
  47. Zemp RJ, Song L, Bitton R, Shung KK, Wang LV. Realtime Photoacoustic Microscopy of Murine Cardiovascular Dynamics. *Optics Express*. 2008 Oct 27.16:18551–18556. [PubMed: 18958134]
  48. Wang X, Pang Y, Ku G, Xie X, Stoica G, Wang LV. Noninvasive laser-induced photoacoustic tomography for structural and functional in vivo imaging of the brain. *Nat Biotech*. 2003; 21:803–806.
  49. Maslov K, Wang LV. Photoacoustic imaging of biological tissue with intensity-modulated continuous-wave laser. *Journal of Biomedical Optics*. 2008; 13:024006. [PubMed: 18465969]
  50. Lashkari B, Mandelis A. Photoacoustic radar imaging signal-to-noise ratio, contrast, and resolution enhancement using nonlinear chirp modulation. *Opt. Lett*. 2010; 35:1623–1625. [PubMed: 20479829]
  51. Lashkari B, Mandelis A. Comparison between pulsed laser and frequency-domain photoacoustic modalities: Signal-to-noise ratio, contrast, resolution, and maximum depth detectivity. *Review of Scientific Instruments*. 2011 Sep.82

52. Paproski RJ, Forbrich AE, Wachowicz K, Hitt MM, Zemp RJ. Tyrosinase as a dual reporter gene for both photoacoustic and magnetic resonance imaging. *Biomedical Optics Express*. 2011 Apr 1.2:771–780. [PubMed: 21483602]
53. Wang LV. Tutorial on Photoacoustic Microscopy and Computed Tomography. *Selected Topics in Quantum Electronics, IEEE Journal of*. 2008; 14:171–179.
54. Krumholz A, Vanvickle-Chavez SJ, Yao J, Fleming TP, Gillanders WE, Wang LV. Photoacoustic microscopy of tyrosinase reporter gene in vivo. *Journal of Biomedical Optics*. 2011 Aug. 16:080503. [PubMed: 21895303]
55. Pramanik M, Wang LV. Thermoacoustic and photoacoustic sensing of temperature. *Journal of Biomedical Optics*. 2009 Sep-Oct;14
56. Wang L, Xia J, Yao J, Maslov KI, Wang LV. Ultrasonically Encoded Photoacoustic Flowgraphy in Biological Tissue. *Physical Review Letters*. 2013; 111:204301. [PubMed: 24289689]
57. Xu MH, Wang LHV. Photoacoustic imaging in biomedicine. *Review of Scientific Instruments*. 2006 Apr.77:22.
58. Xu M, Wang LV. Universal back-projection algorithm for photoacoustic computed tomography. *Physical Review E*. 2005; 71:016706.
59. Finch, D.; Haltmeier, M.; Rakesh. *Inversion of Spherical Means and the Wave Equation in Even Dimensions*. Vol. 68. SIAM: 2007.
60. Burgholzer P, Matt GJ, Haltmeier M, Paltauf Gn. Exact and approximative imaging methods for photoacoustic tomography using an arbitrary detection surface. *Physical Review E*. 2007; 75:046706.
61. Xu Y, Wang LV. Time Reversal and Its Application to Tomography with Diffracting Sources. *Physical Review Letters*. 2004; 92:033902. [PubMed: 14753876]
62. Beard P. Biomedical photoacoustic imaging. *Interface Focus*. 2011 Aug.1:602–631. [PubMed: 22866233]
63. Yulia H, Peter K, Linh N. Reconstruction and time reversal in thermoacoustic tomography in acoustically homogeneous and inhomogeneous media. *Inverse Problems*. 2008; 24:055006.
64. Treeby BE, Cox BT. k-Wave: MATLAB toolbox for the simulation and reconstruction of photoacoustic wave fields. *Journal of Biomedical Optics*. 2010 Mar-Apr;15
65. Xu MH, Wang LV. Analytic explanation of spatial resolution related to bandwidth and detector aperture size in thermoacoustic or photoacoustic reconstruction. *Physical Review E*. 2003 May. 67:15.
66. Wang K, Su R, Oraevsky AA, Anastasio MA. Investigation of iterative image reconstruction in three-dimensional optoacoustic tomography. *Physics in Medicine and Biology*. 2012 Sep.57:5399–5423. [PubMed: 22864062]
67. Wang K, Ermilov SA, Su R, Brecht HP, Oraevsky AA, Anastasio MA. An Imaging Model Incorporating Ultrasonic Transducer Properties for Three-Dimensional Optoacoustic Tomography. *Ieee Transactions on Medical Imaging*. 2011 Feb.30:203–214. [PubMed: 20813634]
68. Xu Y, Wang LV, Ambartsoumian G, Kuchment P. Reconstructions in limited-view thermoacoustic tomography. *Medical Physics*. 2004 Apr.31:724–733. [PubMed: 15124989]
69. Guo Z, Li C, Song L, Wang LV. Compressed sensing in photoacoustic tomography in vivo. *Journal of Biomedical Optics*. 2010; 15:021311. [PubMed: 20459233]
70. Huang B, Xia J, Maslov K, Wang LV. Improving limited-view photoacoustic tomography with an acoustic reflector. *Journal of Biomedical Optics*. 2013; 18:110505–110505. [PubMed: 24285421]
71. Provost J, Lesage F. The Application of Compressed Sensing for Photo-Acoustic Tomography. *Ieee Transactions on Medical Imaging*. 2009 Apr.28:585–594. [PubMed: 19272991]
72. Wang Y, Erpelding TN, Jankovic L, Guo Z, Robert J-L, David G, Wang LV. In vivo three-dimensional photoacoustic imaging based on a clinical matrix array ultrasound probe. *Journal of Biomedical Optics*. 2012; 17:061208–061201. [PubMed: 22734738]
73. Zhang E, Laufer J, Beard P. Backward-mode multiwavelength photoacoustic scanner using a planar Fabry-Perot polymer film ultrasound sensor for high-resolution three-dimensional imaging of biological tissues. *Appl. Opt*. 2008; 47:561–577. [PubMed: 18239717]

74. Laufer J, Zhang E, Raivich G, Beard P. Three-dimensional noninvasive imaging of the vasculature in the mouse brain using a high resolution photoacoustic scanner. *Appl. Opt.* 2009; 48:D299–D306. [PubMed: 19340121]
75. Laufer J, Norris F, Cleary J, Zhang E, Treeby B, Cox B, Johnson P, Scambler P, Lythgoe M, Beard P. In vivo photoacoustic imaging of mouse embryos. *Journal of Biomedical Optics.* 2012; 17:061220–061221. [PubMed: 22734750]
76. Xia J, Guo Z, Maslov K, Aguirre A, Zhu Q, Percival C, Wang LV. Three-dimensional photoacoustic tomography based on the focal-line concept. *Journal of Biomedical Optics.* 2011; 16:090505. [PubMed: 21950908]
77. Buehler A, Herzog E, Razansky D, Ntziachristos V. Video rate optoacoustic tomography of mouse kidney perfusion. *Opt. Lett.* 2010; 35:2475–2477. [PubMed: 20634868]
78. Xia J, Chatni M, Maslov K, Guo Z, Wang K, Anastasio M, Wang LV. Whole-body ring-shaped confocal photoacoustic computed tomography of small animals in vivo. *Journal of Biomedical Optics.* 2012; 17:050506. [PubMed: 22612121]
79. Xia J, Chen W, Maslov K, Anastasio MA, Wang LV. Retrospective respiration-gated whole-body photoacoustic computed tomography of mice. *Journal of Biomedical Optics.* 2014; 19:016003–016003.
80. Kruger RA, Kiser WL, Reinecke DR, Kruger GA, Miller KD. Thermoacoustic Molecular Imaging of Small Animals. *Molecular Imaging.* 2003; 2:113–123. [PubMed: 12964308]
81. Brecht H-P, Su R, Fronheiser M, Ermilov SA, Conjusteau A, Oraevsky AA. Whole-body three-dimensional optoacoustic tomography system for small animals. *Journal of Biomedical Optics.* 2009; 14:064007–064008. [PubMed: 20059245]
82. Kruger R, Reinecke D, Kruger G, Thornton M, Picot P, Morgan T, Stantz K, Mistretta C. HYPR-spectral photoacoustic CT for preclinical imaging. *Proceedings of SPIE.* 2009; 7177:71770F.
83. Kruger RA, Kuzmiak CM, Lam RB, Reinecke DR, Del Rio SP, Steed D. Dedicated 3D photoacoustic breast imaging. *Medical Physics.* 2013; 40
84. Xu, M. *Photoacoustic Imaging and Spectroscopy.* CRC Press: 2009. Analysis of Spatial Resolution in Photoacoustic Tomography; p. 47-60.vol. null
85. Yao JJ, Wang LHV. Photoacoustic microscopy. *Laser & Photonics Reviews.* 2013 Sep.7:758–778.
86. Hu S, Maslov K, Wang LV. Second-generation optical-resolution photoacoustic microscopy with improved sensitivity and speed. *Optics Letters.* 2011 Apr 1.36:1134–1136. [PubMed: 21479007]
87. Maslov K, Zhang HF, Hu S, Wang LV. Optical-resolution photoacoustic microscopy for in vivo imaging of single capillaries. *Optics Letters.* 2008 May 1.33:929–931. [PubMed: 18451942]
88. Maslov K, Stoica G, Wang LHV. In vivo dark-field reflection-mode photoacoustic microscopy. *Optics Letters.* 2005 Mar 15.30:625–627. [PubMed: 15791997]
89. Yang JM, Favazza C, Chen RM, Yao JJ, Cai X, Maslov K, Zhou QF, Shung KK, Wang LHV. Simultaneous functional photoacoustic and ultrasonic endoscopy of internal organs in vivo. *Nature Medicine.* 2012 Aug.18:1297-+.
90. Hajireza P, Shi W, Zemp R. Label-free in vivo GRIN-lens optical resolution photoacoustic micro-endoscopy. *Laser Physics Letters.* 2013 May.10
91. Yang JM, Chen RM, Favazza C, Yao JJ, Li CY, Hu ZL, Zhou QF, Shung KK, Wang LV. A 2.5-mm diameter probe for photoacoustic and ultrasonic endoscopy. *Optics Express.* 2012 Oct 8.20:23944–23953. [PubMed: 23188360]
92. Shao P, Shi W, Hajireza P, Zemp RJ. Integrated micro-endoscopy system for simultaneous fluorescence and optical-resolution photoacoustic imaging. *Journal of Biomedical Optics.* 2012 Jul.17
93. Yang JM, Maslov K, Yang HC, Zhou QF, Shung KK, Wang LHV. Photoacoustic endoscopy. *Optics Letters.* 2009 May 15.34:1591–1593. [PubMed: 19448831]
94. Xing WX, Wang LD, Maslov K, Wang LHV. Integrated optical- and acoustic-resolution photoacoustic microscopy based on an optical fiber bundle. *Optics Letters.* 2013 Jan 1.38:52–54. [PubMed: 23282835]
95. Xu X, Liu H, Wang LV. Time-reversed ultrasonically encoded optical focusing into scattering media. *Nature Photonics.* 2011; 5:154–157. [PubMed: 21532925]

96. Judkewitz B, Wang YM, Horstmeyer R, Mathy A, Yang C. Speckle-scale focusing in the diffusive regime with time reversal of variance-encoded light (TROVE). *Nat Photon*. 2013; 7:300–305.
97. Li L, Zemp RJ, Lungu G, Stoica G, Wang LV. Photoacoustic imaging of lacZ gene expression in vivo. *Journal of Biomedical Optics*. 2007; 12:020504–020503. [PubMed: 17477703]
98. Krüger A, Schirmmayer V, Khokha R. The bacterial lacZ gene: An important tool for metastasis research and evaluation of new cancer therapies. *Cancer and Metastasis Reviews*. 1998 Sep 01; 17:285–294. 1998. [PubMed: 10352882]
99. Cai X, Li L, Krumholz A, Guo ZJ, Erpelding TN, Zhang C, Zhang Y, Xi YN, Wang LHV. Multi-Scale Molecular Photoacoustic Tomography of Gene Expression. *Plos One*. 2012 Aug 27.7
100. Xia J, Li G, Wang L, Nasirivanaki M, Maslov K, Engelbach JA, Garbow JR, Wang LV. Wide-field two-dimensional multifocal optical-resolution photoacoustic-computed microscopy. *Optics Letters*. 2013 Dec 15; 38:5236–5239. 2013. [PubMed: 24322226]
101. Huang B, Bates M, Zhuang XW. Super-Resolution Fluorescence Microscopy. *Annual Review of Biochemistry*. 2009; 78:993–1016.
102. Yao J, Wang L, Li C, Zhang C, Wang LV. Photoimprint Photoacoustic Microscopy for Three-Dimensional Label-Free Subdiffraction Imaging. *Physical Review Letters*. 2014; 112:014302. [PubMed: 24483902]
103. Nedosekin DA, Galanzha EI, Dervishi E, Biris AS, Zharov VP. Super-resolution nonlinear photothermal microscopy. *Small*. 2014 Jan 15; 10:135–142. [PubMed: 23864531]
104. Conkey, Donald B.; Caravaca-Aguirre, Antonio M.; Dove, Jacob D.; Ju, Hengyi; Murray, Todd W.; Piestun, R. Super-resolution photoacoustic imaging through a scattering wall. arXiv. 2013; 1310.5736
105. Lai P, Wang L, Tay JW, Wang L. Nonlinear photoacoustic wavefront shaping (PAWS) for single speckle-grain optical focusing in scattering media. arXiv. 2014 arXiv:1402.0816.
106. Hanahan D, Weinberg RA. Hallmarks of Cancer: The Next Generation. *Cell*. 2011 Mar 4; 144:646–674. [PubMed: 21376230]
107. Zhang HF, Maslov K, Sivaramakrishnan M, Stoica G, Wang LHV. Imaging of hemoglobin oxygen saturation variations in single vessels in vivo using photoacoustic microscopy. *Applied Physics Letters*. 2007 Jan 29; 90:053901.
108. Maslov K, Zhang HF, Wang LV. Effects of wavelength-dependent fluence attenuation on the noninvasive photoacoustic imaging of hemoglobin oxygen saturation in subcutaneous vasculature in vivo. *Inverse Problems*. 2007 Dec. 23:S113–S122.
109. Hu S, Maslov K, Wang LHV. Noninvasive label-free imaging of microhemodynamics by optical-resolution photoacoustic microscopy. *Optics Express*. 2009 Apr 27; 17:7688–7693. [PubMed: 19399148]
110. Hu S, Maslov K, Wang LHV. In vivo functional chronic imaging of a small animal model using optical-resolution photoacoustic microscopy. *Medical Physics*. 2009 Jun; 36:2320–2323. [PubMed: 19610320]
111. Hu S, Rao B, Maslov K, Wang LV. Label-free photoacoustic ophthalmic angiography. *Optics Letters*. 2010 Jan 1; 35:1–3. [PubMed: 20664653]
112. Wang Y, Maslov K, Wang LHV. Spectrally encoded photoacoustic microscopy using a digital mirror device. *Journal of Biomedical Optics*. 2012 Jun; 17:066020. [PubMed: 22734776]
113. Ranasinghesagara JC, Zemp RJ. Combined photoacoustic and oblique-incidence diffuse reflectance system for quantitative photoacoustic imaging in turbid media. *Journal of Biomedical Optics*. 2010 Jul-Aug; 15:046016. [PubMed: 20799818]
114. Bauer AQ, Nothdurft RE, Erpelding TN, Wang LHV, Culver JP. Quantitative photoacoustic imaging: correcting for heterogeneous light fluence distributions using diffuse optical tomography. *Journal of Biomedical Optics*. 2011 Sep; 16:096016. [PubMed: 21950930]
115. Guo Z, Favazza C, Garcia-Urbe A, Wang LV. Quantitative photoacoustic microscopy of optical absorption coefficients from acoustic spectra in the optical diffusive regime. *Journal of Biomedical Optics*. 2012; 17:066011–066011. [PubMed: 22734767]
116. Guo Z, Hu S, Wang LV. Calibration-free absolute quantification of optical absorption coefficients using acoustic spectra in 3D photoacoustic microscopy of biological tissue. *Opt. Lett*. 2010; 35:2067–2069. [PubMed: 20548388]

117. Xia J, Danielli A, Liu Y, Wang L, Maslov K, Wang LV. Calibration-free quantification of absolute oxygen saturation based on the dynamics of photoacoustic signals. *Opt. Lett.* 2013; 38:2800–2803. [PubMed: 23903146]
118. Wang RK, Hurst S. Mapping of cerebro-vascular blood perfusion in mice with skin and skull intact by Optical Micro-AngioGraphy at 1.3  $\mu$ m wavelength. *Optics Express.* 2007 Sep 3.15:11402–11412. [PubMed: 19547498]
119. An L, Wang RK. In vivo volumetric imaging of vascular perfusion within human retina and choroids with optical micro-angiography. *Optics Express.* 2008 Jul 21.16:11438–11452. [PubMed: 18648464]
120. Cobbold, RSC. Foundations of biomedical ultrasound. Oxford ; New York: Oxford University Press; 2007.
121. Fang H, Maslov K, Wang LV. Photoacoustic Doppler flow measurement in optically scattering media. *Applied Physics Letters.* 2007 Dec 24.91:264103.
122. Sheinfeld, A.; Gilead, S.; Eyal, A. Photons Plus Ultrasound: Imaging and Sensing 2010. San Francisco, California, USA: 2010. Time-resolved photoacoustic Doppler characterization of flow using pulsed excitation; p. 75643N-6
123. Fang H, Wang LHV. M-mode photoacoustic particle flow imaging. *Optics Letters.* 2009 Mar 1.34:671–673. [PubMed: 19252588]
124. Yao J, Maslov KI, Shi Y, Taber LA, Wang LV. In vivo photoacoustic imaging of transverse blood flow by using Doppler broadening of bandwidth. *Optics Letters.* 2010 May 1.35:1419–1221. [PubMed: 20436589]
125. Yao JJ, Wang LHV. Transverse flow imaging based on photoacoustic Doppler bandwidth broadening. *Journal of Biomedical Optics.* 2010 Mar-Apr;15:021304. [PubMed: 20459226]
126. Yao J, Maslov KI, Wang LV. In vivo Photoacoustic Tomography of Total Blood Flow and Potential Imaging of Cancer Angiogenesis and Hypermetabolism. *Technology in cancer research & treatment.* 2012 Mar 15.
127. Brunker, J.; Beard, P. Photons Plus Ultrasound: Imaging and Sensing 2010. San Francisco: 2010. Pulsed photoacoustic Doppler flowmetry using a cross correlation method; p. 756426
128. Sheinfeld A, Eyal A. Photoacoustic thermal diffusion flowmetry. *Biomedical Optics Express.* 2012 Apr 1.3:800–813. [PubMed: 22574267]
129. Wei C, Huang SW, Wang CRC, Li PC. Photoacoustic flow measurements based on wash-in analysis of gold nanorods. *Ieee Transactions on Ultrasonics Ferroelectrics and Frequency Control.* 2007 Jun.54:1131–1141.
130. Wei CW, Liao CK, Tseng HC, Lin YP, Chen CC, Li PC. Photoacoustic flow measurements with gold nanoparticles. *Ieee Transactions on Ultrasonics Ferroelectrics and Frequency Control.* 2006 Oct.53:1955–1959.
131. Song L, Maslov K, Wang LV. Section-illumination photoacoustic microscopy for dynamic 3D imaging of microcirculation in vivo. *Optics Letters.* 2010 May 1.35:1482–1484. [PubMed: 20436610]
132. Zhang R, Yao J, Maslov KI, Wang LV. Structured-illumination photoacoustic Doppler flowmetry of axial flow in homogeneous scattering media. *Applied Physics Letters.* 2013 Aug 26.103:94101. [PubMed: 24065864]
133. Wang L, Yao J, Maslov KI, Xing W, Wang LV. Ultrasound-heated photoacoustic flowmetry. *Journal of Biomedical Optics.* 2013 Nov 1.18:117003. [PubMed: 24194064]
134. Hanahan D, Weinberg RA. The hallmarks of cancer. *Cell.* 2000 Jan 7.100:57–70. [PubMed: 10647931]
135. Wang LV. Prospects of photoacoustic tomography. *Medical Physics.* 2008 Dec.35:5758–5767. [PubMed: 19175133]
136. Liu T, Wei Q, Wang J, Jiao SL, Zhang HF. Combined photoacoustic microscopy and optical coherence tomography can measure metabolic rate of oxygen. *Biomedical Optics Express.* 2011 May 1.2:1359–1365. [PubMed: 21559147]
137. Jiang Y, Forbrich A, Harrison T, Zemp RJ. Blood oxygen flux estimation with a combined photoacoustic and high-frequency ultrasound microscopy system: a phantom study. *Journal of Biomedical Optics.* 2012; 17:036012. [PubMed: 22502570]

138. Wang LD, Maslov K, Wang LHV. Single-cell label-free photoacoustic flowoxigraphy in vivo. *Proceedings of the National Academy of Sciences of the United States of America*. 2013 Apr 9.110:5759–5764. [PubMed: 23536296]
139. MacKenzie HA, Ashton HS, Spiers S, Shen YC, Freeborn SS, Hannigan J, Lindberg J, Rae P. Advances in photoacoustic noninvasive glucose testing. *Clinical Chemistry*. 1999 Sep.45:1587–1595. [PubMed: 10471673]
140. Gao L, Zhang C, Li CY, Wang LHV. Intracellular temperature mapping with fluorescence-assisted photoacoustic-thermometry. *Applied Physics Letters*. 2013 May 13.102
141. Wang HW, Chai N, Wang P, Hu S, Dou W, Umulis D, Wang LHV, Sturek M, Lucht R, Cheng JX. Label-Free Bond-Selective Imaging by Listening to Vibrationally Excited Molecules. *Physical Review Letters*. 2011 Jun 10.106:238106. [PubMed: 21770549]
142. Yakovlev VV, Zhang HF, Noojin GD, Denton ML, Thomas RJ, Scully MO. Stimulated Raman photoacoustic imaging. *Proceedings of the National Academy of Sciences of the United States of America*. 2010 Nov.107:20335–20339. [PubMed: 21059930]
143. Wang Y, Wang LV. Förster resonance energy transfer photoacoustic microscopy. *Journal of Biomedical Optics*. 2012; 17:086007. [PubMed: 23224194]
144. Wang Y, Xia J, Wang LV. Deep-tissue photoacoustic tomography of Förster resonance energy transfer. *Journal of Biomedical Optics*. 2013; 18:101316–101316. [PubMed: 23884608]
145. Danielli A, Favazza CP, Maslov K, Wang LV. Picosecond absorption relaxation measured with nanosecond laser photoacoustics. *Applied Physics Letters*. 2010 Oct 18.97:163701. [PubMed: 21079726]
146. Danielli A, Favazza CP, Maslov K, Wang LHV. Single-wavelength functional photoacoustic microscopy in biological tissue. *Optics Letters*. 2011 Mar 1.36:769–771. [PubMed: 21368977]
147. Hu, S.; Maslov, K.; Yan, P.; Lee, J.-M.; Wang, LV. *Photons Plus Ultrasound: Imaging and Sensing 2012*. San Francisco, California, USA: 2012. Dichroism optical-resolution photoacoustic microscopy; p. 82233T-4
148. Xia J, Pelivanov I, Wei C, Hu X, Gao X, O'Donnell M. Suppression of background signal in magnetomotive photoacoustic imaging of magnetic microspheres mimicking targeted cells. *Journal of Biomedical Optics*. 2012; 17:061224. [PubMed: 22734754]
149. Ray A, Rajian JR, Lee Y-EK, Wang X, Kopelman R. Lifetime-based photoacoustic oxygen sensing in vivo. *Journal of Biomedical Optics*. 2012; 17:057004. [PubMed: 22612143]
150. Chatni MR, Yao JJ, Danielli A, Favazza CP, Maslov KI, Wang LHV. Functional photoacoustic microscopy of pH. *Journal of Biomedical Optics*. 2011 Oct.16:100503. [PubMed: 22029342]
151. Ashkenazi S, Huang SW, Horvath T, Koo YE, Kopelman R. Photoacoustic probing of fluorophore excited state lifetime with application to oxygen sensing. *Journal of Biomedical Optics*. 2008 May-Jun;13:034023. [PubMed: 18601568]
152. Ashkenazi S. Photoacoustic lifetime imaging of dissolved oxygen using methylene blue. *Journal of Biomedical Optics*. 2010 Jul-Aug;15:040501. [PubMed: 20799768]
153. Wilson KE, Wang TY, Willmann JK. Acoustic and Photoacoustic Molecular Imaging of Cancer. *Journal of Nuclear Medicine*. 2013 Nov 1.54:1851–1854. [PubMed: 24187042]
154. de la Zerda A, Kim JW, Galanzha EI, Gambhir SS, Zharov VP. Advanced contrast nanoagents for photoacoustic molecular imaging, cytometry, blood test and photothermal theranostics. *Contrast Media & Molecular Imaging*. 2011 Sep-Oct;6:346–369. [PubMed: 22025336]
155. Yang XM, Stein EW, Ashkenazi S, Wang LHV. Nanoparticles for photoacoustic imaging. *Wiley Interdisciplinary Reviews-Nanomedicine and Nanobiotechnology*. 2009 Jul-Aug;1:360–368. [PubMed: 20049803]
156. Luke GP, Yeager D, Emelianov SY. Biomedical applications of photoacoustic imaging with exogenous contrast agents. *Annals of biomedical engineering*. 2012 Feb.40:422–437. [PubMed: 22048668]
157. Kim C, Favazza C, Wang LHV. In Vivo Photoacoustic Tomography of Chemicals: High-Resolution Functional and Molecular Optical Imaging at New Depths. *Chemical Reviews*. 2010 May.110:2756–2782. [PubMed: 20210338]
158. Kircher MF, de la Zerda A, Jokerst JV, Zavaleta CL, Kempen PJ, Mitra E, Pitter K, Huang RM, Campos C, Habte F, Sinclair R, Brennan CW, Mellinghoff IK, Holland EC, Gambhir SS. A brain

- tumor molecular imaging strategy using a new triple-modality MRI-photoacoustic-Raman nanoparticle. *Nature Medicine*. 2012 May.18:829–U235.
159. Ray A, Wang XD, Lee YEK, Hah HJ, Kim G, Chen T, Orringer DA, Sagher O, Liu XJ, Kopelman R. Targeted blue nanoparticles as photoacoustic contrast agent for brain tumor delineation. *Nano Research*. 2011 Nov.4:1163–1173.
160. Razansky D, Baeten J, Ntziachristos V. Sensitivity of molecular target detection by multispectral optoacoustic tomography (MSOT). *Medical Physics*. 2009 Mar.36:939–945. [PubMed: 19378754]
161. Laufer J, Jathoul A, Pule M, Beard P. In vitro characterization of genetically expressed absorbing proteins using photoacoustic spectroscopy. *Biomedical Optics Express*. 2013 Nov 1.4:2477–2490. [PubMed: 24298408]
162. Krumholz A, Shcherbakova DM, Xia J, Wang LV, Verkhusha VV. Multicontrast photoacoustic in vivo imaging using near-infrared fluorescent proteins. *Sci. Rep.* 2014; 4
163. Laufer, J.; Jathoul, A.; Johnson, P.; Zhang, E.; Lythgoe, M.; Pedley, RB.; Pule, M.; Beard, P. *Photons Plus Ultrasound: Imaging and Sensing 2012*. San Francisco, California, USA: 2012. In vivo photoacoustic imaging of tyrosinase expressing tumours in mice; p. 82230M-5
164. Qin CX, Cheng K, Chen K, Hu X, Liu Y, Lan XL, Zhang YX, Liu HG, Xu YD, Bu LH, Su XH, Zhu XH, Meng SX, Cheng Z. Tyrosinase as a multifunctional reporter gene for Photoacoustic/MRI/PET triple modality molecular imaging. *Scientific Reports*. 2013 Mar 19.3:1490. [PubMed: 23508226]
165. Bell, MAL.; Guo, X.; Song, DY.; Boctor, EM. *Photons Plus Ultrasound: Imaging and Sensing 2014*. San Francisco, California, USA: 2014. Photoacoustic imaging of prostate brachytherapy seeds with transurethral light delivery; p. 89430N-89430N-6.
166. Cox B, Laufer JG, Arridge SR, Beard PC. Quantitative spectroscopic photoacoustic imaging: a review. *Journal of Biomedical Optics*. 2012; 17:061202–061201. [PubMed: 22734732]

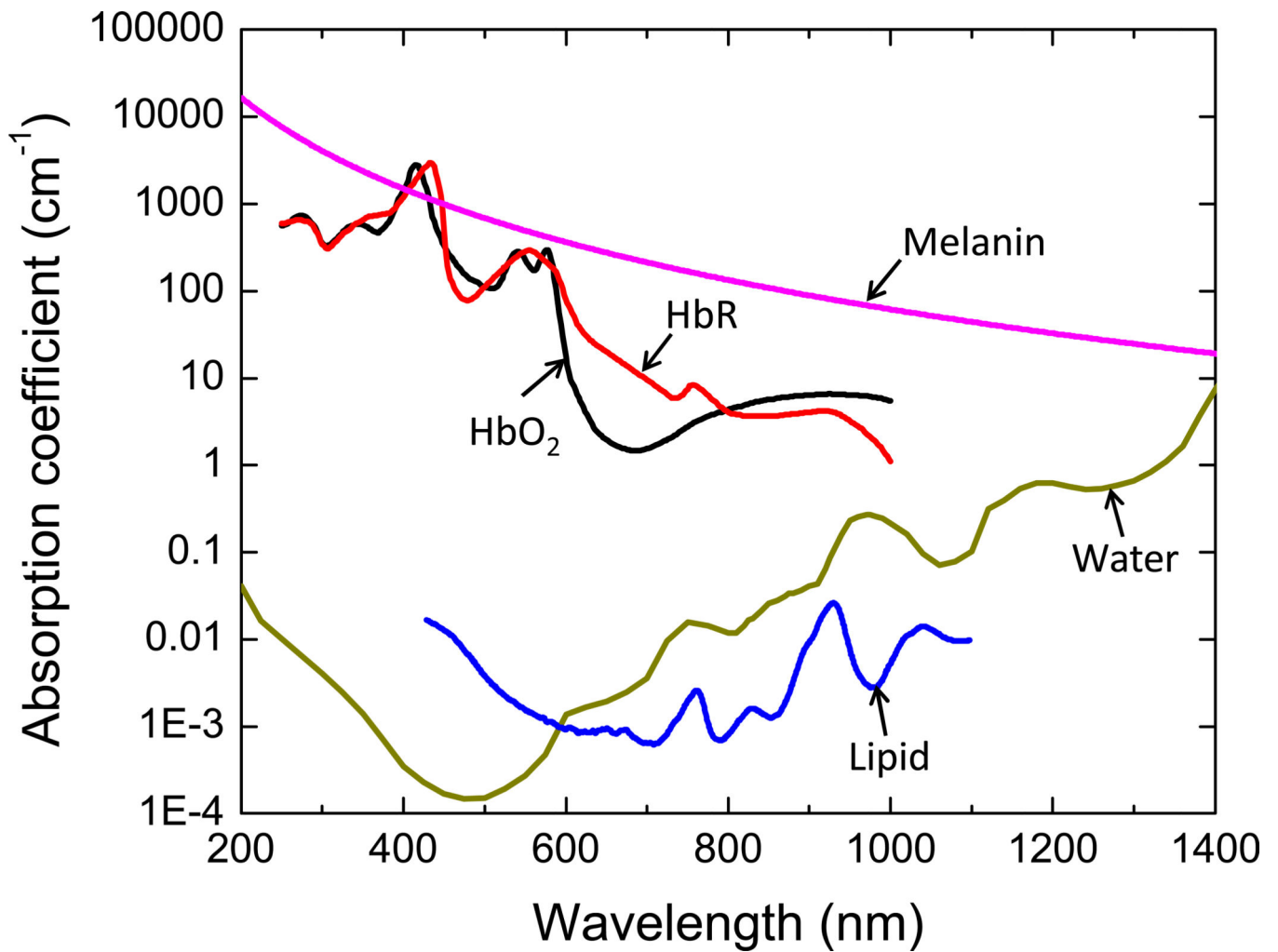


**Figure 1.** Absorption coefficient spectra of endogenous tissue chromophores at their typical concentrations in the human body. Oxy-hemoglobin (HbO<sub>2</sub>) and deoxy-hemoglobin (HbR), 150 gL<sup>-1</sup>. Water, 60% by weight. Lipid, 16% by weight. Melanin concentration corresponds to that in normal skin. Adapted from <http://omlc.ogi.edu>.

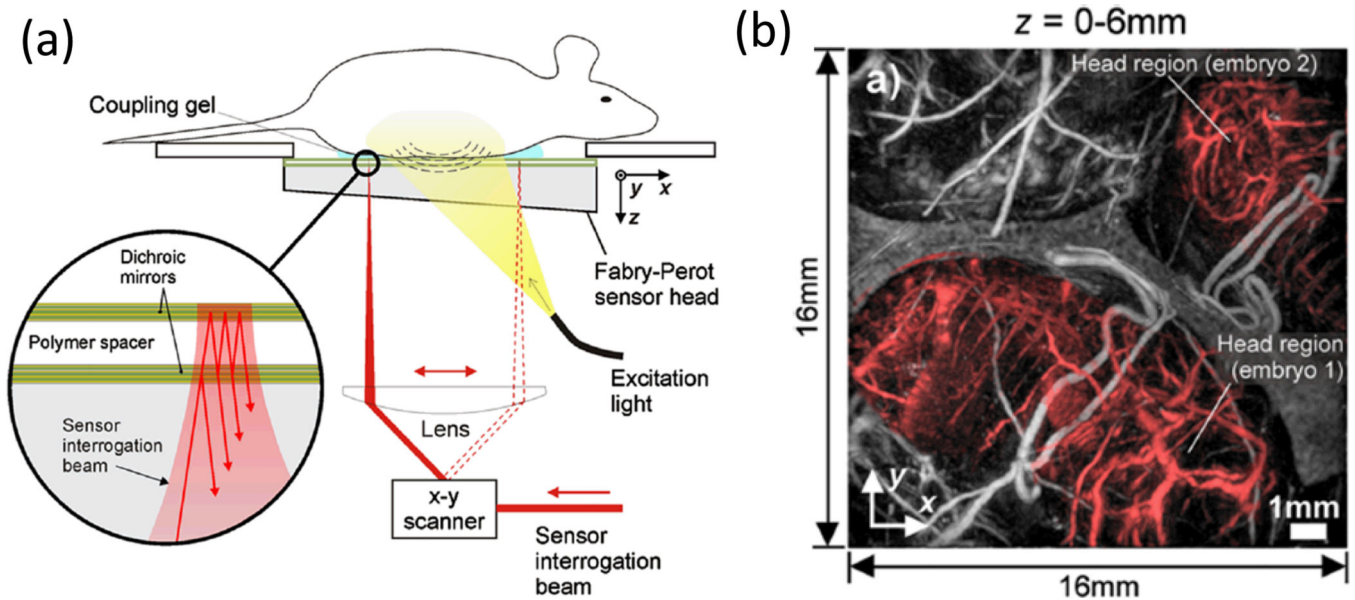


**Figure 2.**

(a) Schematic illustrating the operation of the Fabry-Perot interferometer-based PACT imaging system. Photoacoustic waves are generated by the absorption of nanosecond optical pulses provided by a wavelength-tunable OPO laser and detected by a transparent Fabry-Perot polymer film ultrasound sensor. The sensor comprises a pair of dichroic mirrors separated by a 40  $\mu\text{m}$  thick polymer spacer, thus forming a Fabry-Perot interferometer (FPI). The waves are mapped in 2D by raster-scanning a CW focused interrogation laser beam across the sensor and recording the acoustically induced modulation of the reflectivity of the FPI at each scanning point. (b) Maximum amplitude projection of the complete three dimensional image dataset (depth 0 to 6 mm), showing two embryos (shaded red). Reproduced with permission from [75].

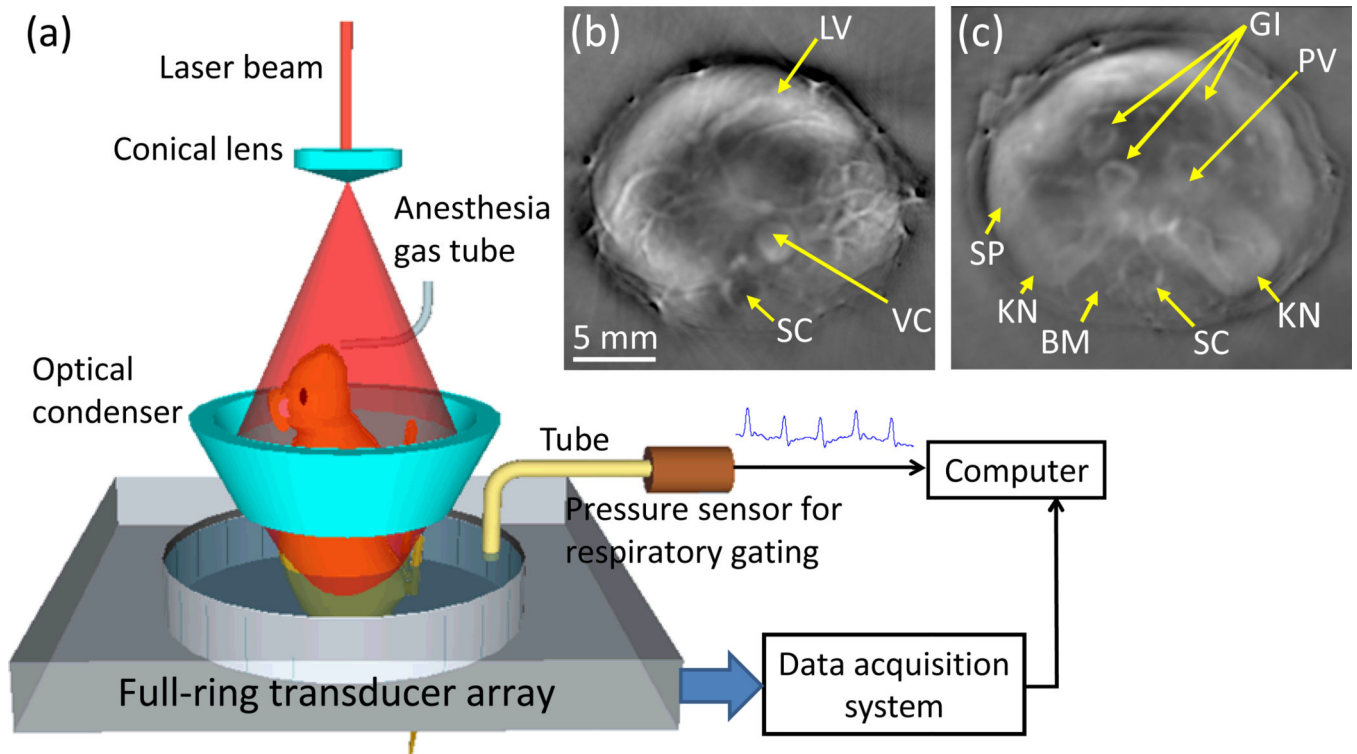


**Figure 3.** (a) Schematic of a ring-shaped confocal photoacoustic computed tomography (RC-PACT) system. (b)–(c) *In vivo* RC-PACT images of athymic mice acquired noninvasively at the (b) liver and (c) kidney regions. BM, backbone muscle; GI, GI tract; KN, kidney; LV, liver; PV, portal vein; SC, spinal cord; SP, spleen; and VC, vena cava. Reproduced with permission from [78, 79].

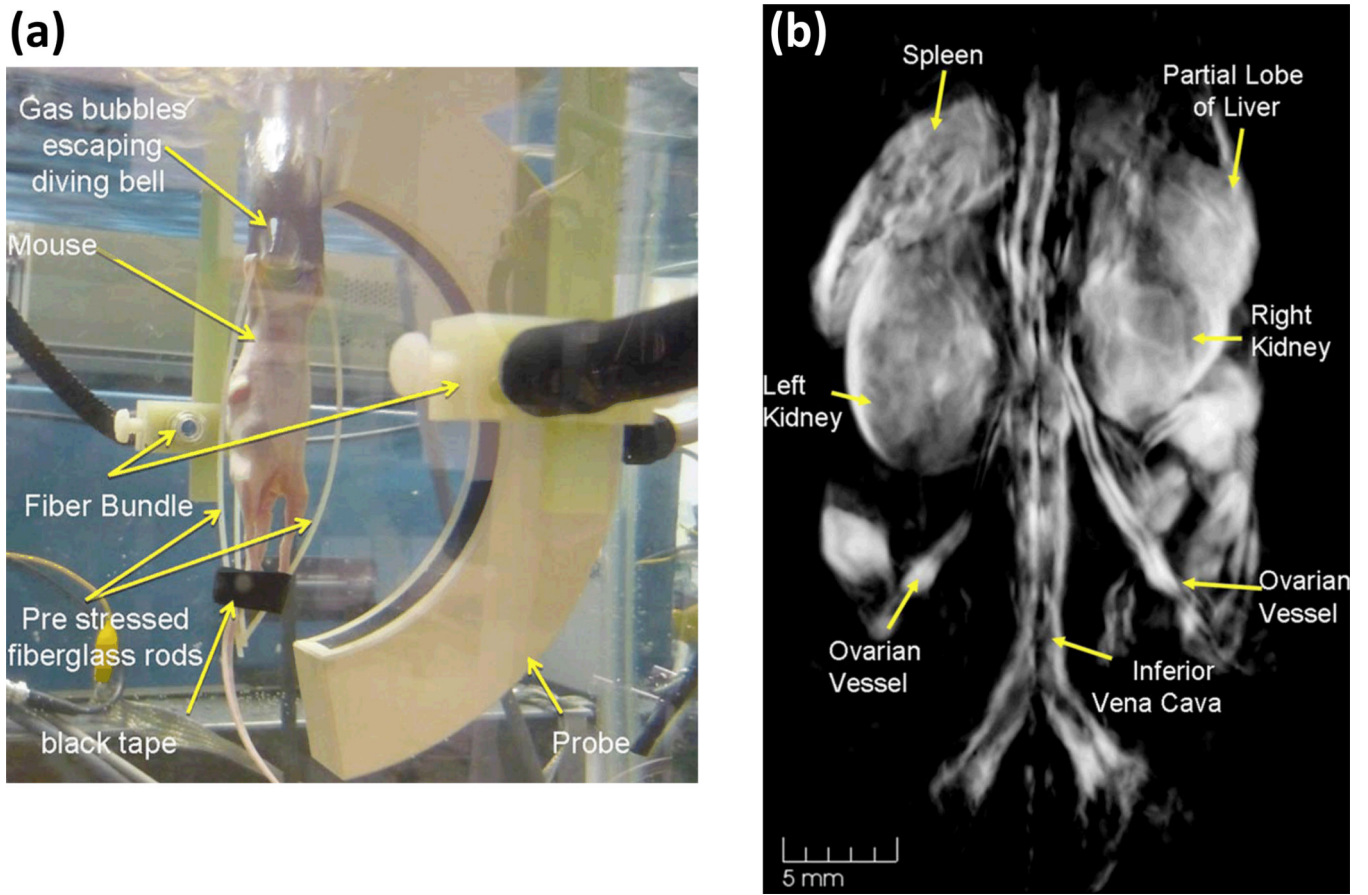


**Figure 4.** (a) Photograph of an arc-array-based spherical-view PACT system. (b) Three-dimensional photoacoustic image of a female nude mouse. Reproduced with permission from [80].

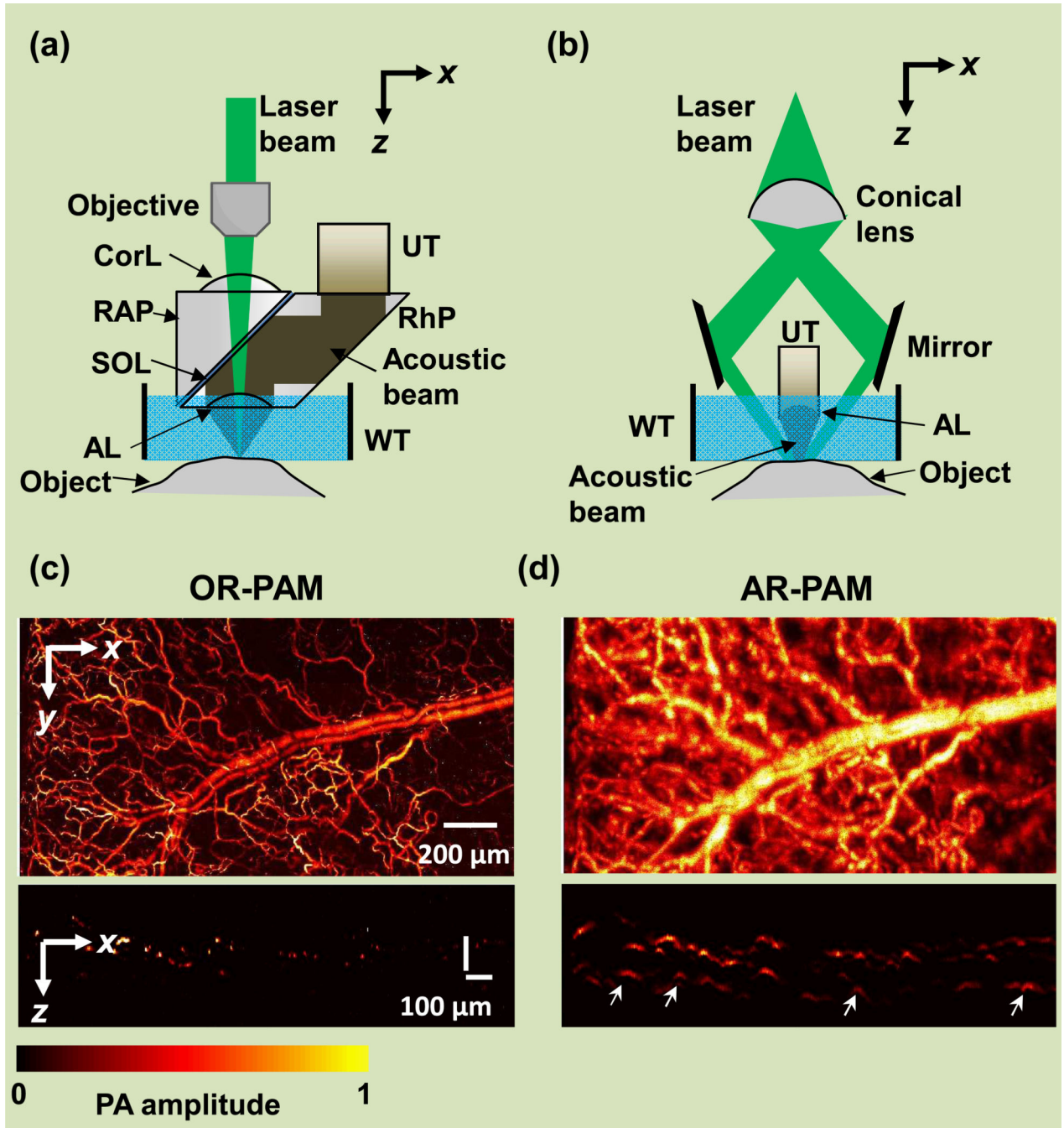


**Figure 5.**

Photoacoustic microscopy (PAM). (a) Second-generation optical-resolution photoacoustic microscopy system (2G-OR-PAM), where the lateral resolution is determined by the diffraction-limited optical focusing. AL, acoustic lens; CorL, correction lens; RAP, right angled prism; RhP, rhomboid prism; SOL, silicone oil layer; UT, ultrasonic transducer; WT, water tank. (b) Dark-field acoustic-resolution photoacoustic microscopy (AR-PAM), where the lateral resolution is determined by the diffraction-limited acoustic focusing. (c–d) *In vivo* label-free mouse ear vasculature imaged by (a) OR-PAM and (b) AR-PAM. A

representative cross-sectional image is shown at the bottom. While OR-PAM shows better resolution, AR-PAM has greater penetration depth (shown by arrows). Reproduced with permission from [94].

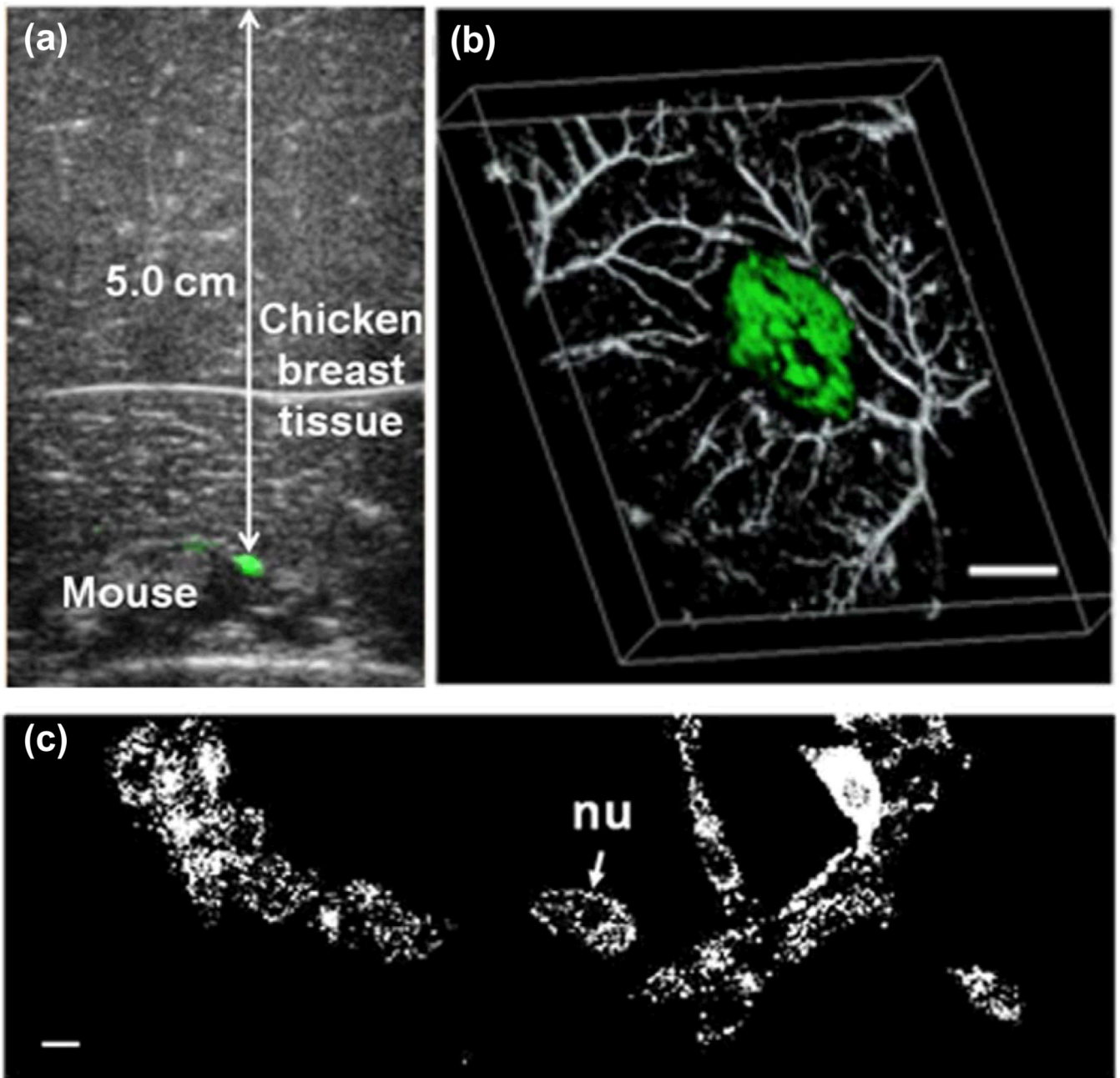


**Figure 6.** Multi-scale photoacoustic images of *LacZ* gene expression. (a) B-scan image of a *lacZ*-marked tumor at a 5-cm depth in biological tissue, acquired by overlaying chicken breast tissue on top of a mouse. Photoacoustic images are colored green, while ultrasonic images are in gray. (b) 3D depiction of a composite photoacoustic image, showing the tumor and blood vessels imaged with AR-PAM. Green: tumor. The scale bar represents 2 mm. (c) An OR-PAM image of fixed *lacZ* cells grown on a cover glass after staining with Xgal. nu: cell nucleus. The scale bar represents 10  $\mu\text{m}$ . Reproduced with permission from [99].

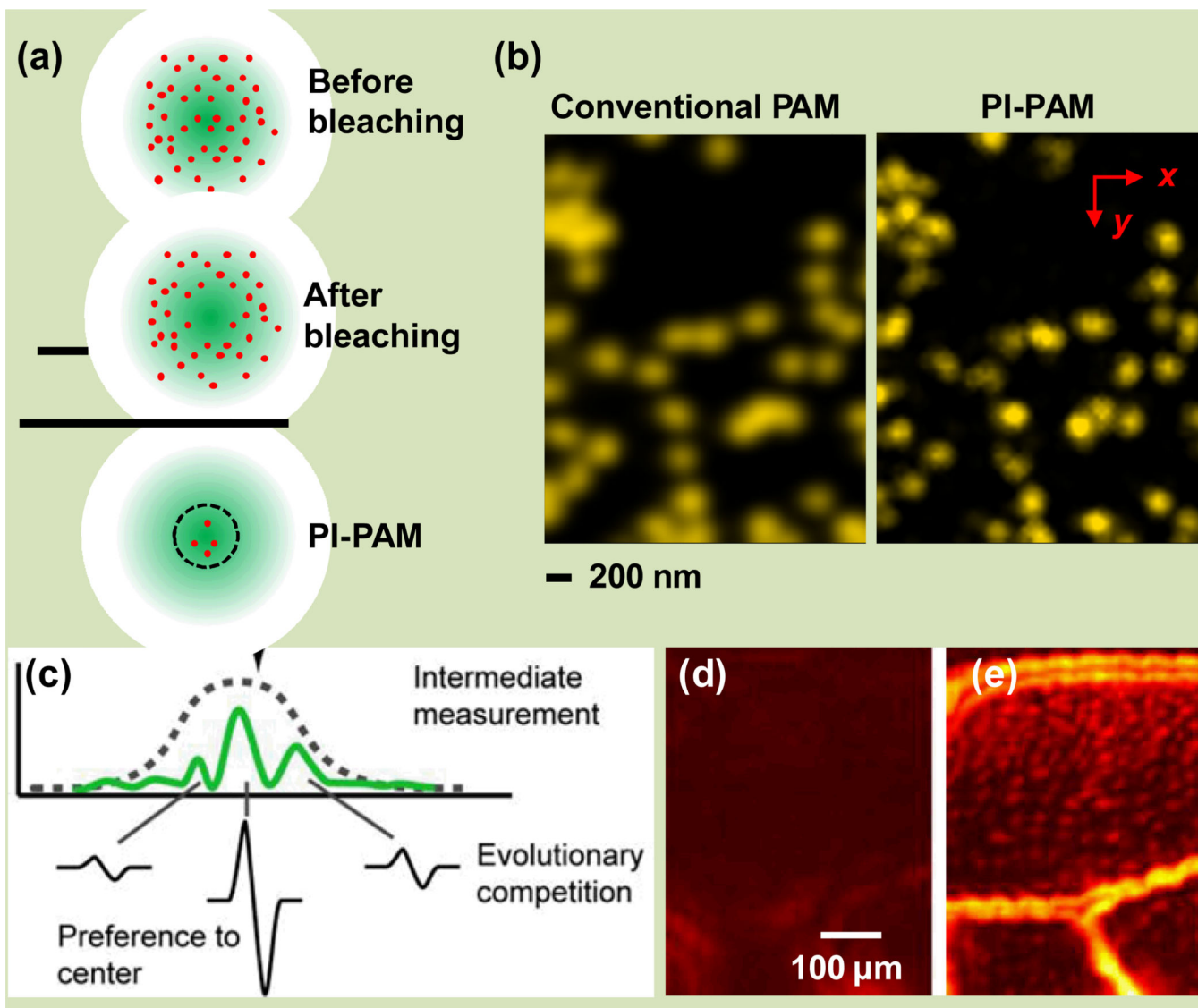


**Figure 7.** Super-resolution photoacoustic microscopy. (a) Photoimprint photoacoustic microscopy (PI-PAM) [102]. Since the photobleaching rate depends on the local excitation intensity, the first excitation bleaches the center part of the illuminated region more than the periphery, leaving an imprint in the sample. The differential signal between before- and after-bleaching images results in a smaller effective excitation size and thus a resolution enhancement, as shown by the dashed circle in the bottom panel. (b) PI-PAM imaging of gold nanoparticles with enhanced lateral resolution. (c) Wavefront-shaping assisted sub-acoustic resolution PA imaging. Each photoacoustic emission from the speckle grains is weighted by the Gaussian detection sensitivity of the acoustic transducer [104]. (d–e) Photoacoustic images of a sweet bee wing created with (d) random optical speckle illumination and (e) wavefront optimized speckle focus, showing the superior resolution of the latter method. Adapted with permission from [102, 104].

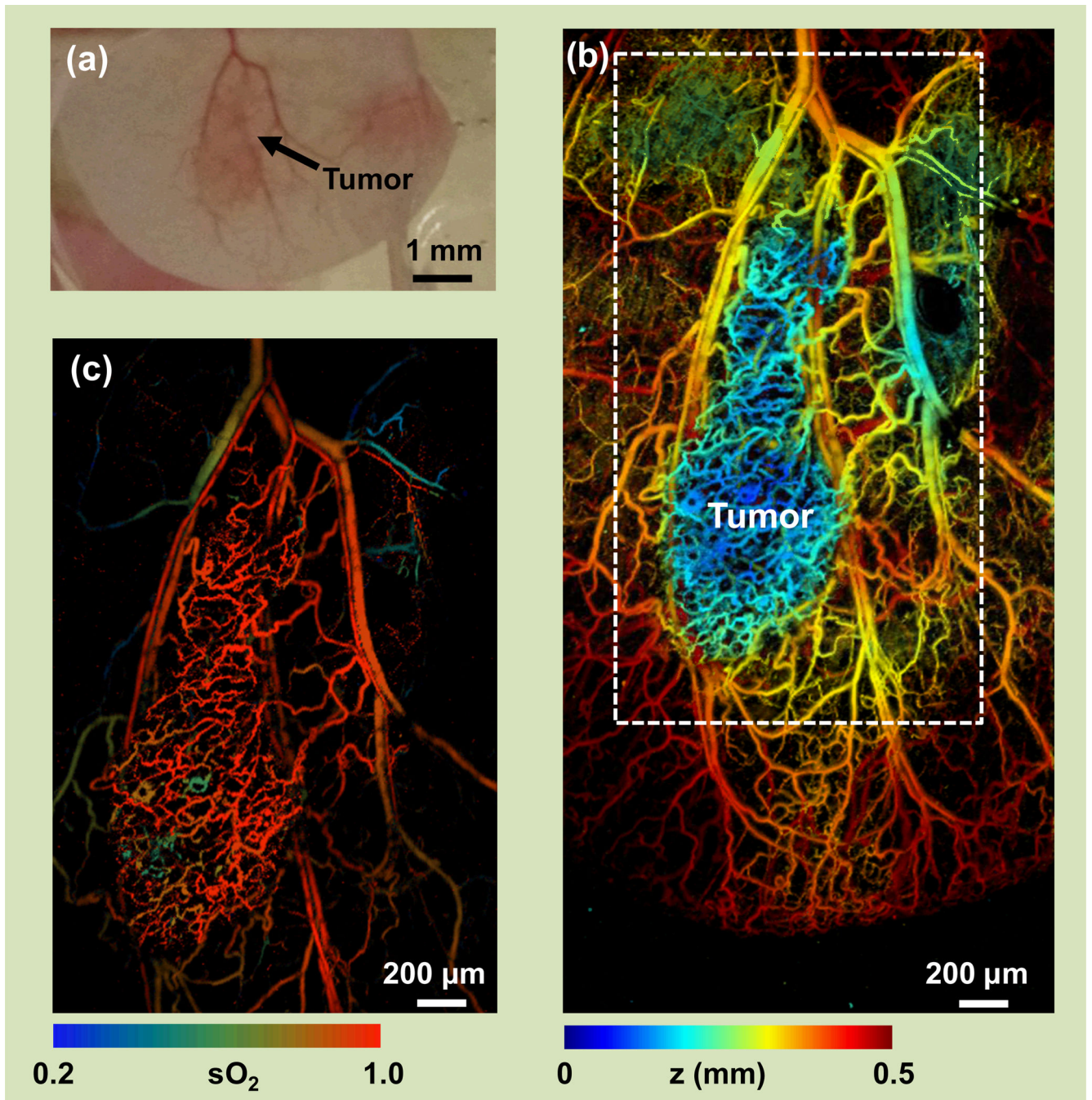


**Figure 8.** Multi-parameter PA imaging. (a) Photograph of a mouse ear bearing a U87 glioblastoma tumor. (b) Depth-encoded vascular image acquired with OR-PAM, showing the tortuous blood vessels in the tumor. (c)  $sO_2$  map of the tumor region, showing the hyperoxic status of the early-stage tumor.

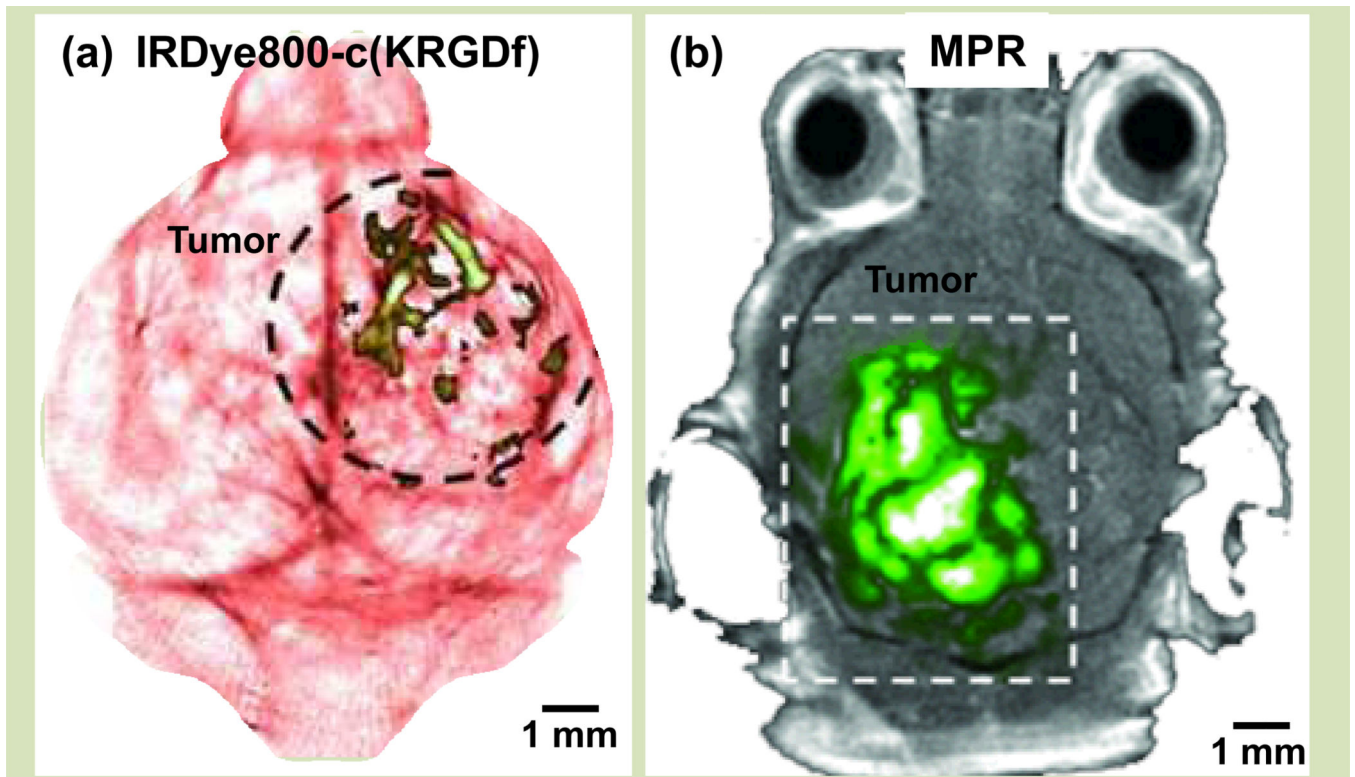


**Figure 9.** Photoacoustic molecular imaging. (a) PACT of a glioblastoma in a mouse brain enhanced by IRDye800-c(KRGDf), which targeted overexpressed integrin  $\alpha_v\beta_3$  in tumor cells. (b) PAT of a glioblastoma in a mouse brain enhanced by tri-modality MRI-PA-Raman (MPR) nanoparticles. Reproduced with permission from [23, 158].